Supporting Information

Materials and Syntheses

Unless otherwise noted, all reagents and solvents were used and received from commercial suppliers. 2,6-dibromoanthraquinone, 2,6-dibromoanthracene, 2,3,6,7,10,11-hexabromotriphenylene, 4-(cyanomethyl)benzeneboronic acid pinacol ester, and 4-formylphenylboronic acid were purchased from Haohong Biomedical Technology Co., Ltd. 1,2-dichlorobenzene (*o*-DCB), methanol (MeOH), N,N-Dimethylformamide (DMF), tetrakis(triphenylphosphine)palladium ($Pd(PPh_3)_4$), and tetrahydrofuran (THF) were purchased from Energy Chemical Reagent Co., Ltd. Tetrabutylammonium hydroxide (TBAH) was purchased from Thermo Fisher Scientific Co., Ltd.

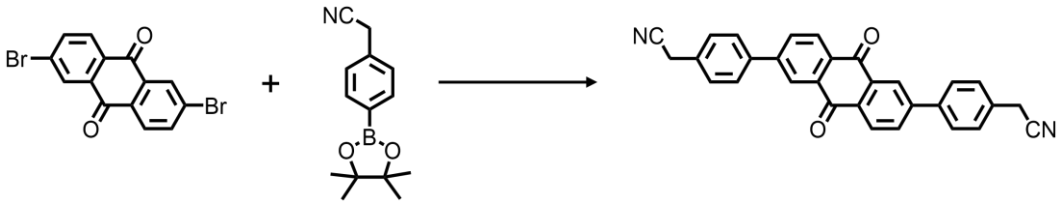

Scheme S1. Synthesis of 2,2'-(anthraquinone-2,6-diylbis(4,1-phenyl))diacetonitrile (AQDAN).

Synthesis of 2,2'-(anthraquinone-2,6-diylbis(4,1-phenyl))diacetonitrile (AQDAN): 2,6-dibromoanthraquinone (366.0 mg, 1 mmol), 4-(cyanomethyl)benzeneboronic acid pinacol ester (607.8 mg, 2.5 mmol), K_2CO_3 (829.3 mg, 6 mmol), and $Pd(PPh_3)_4$ (231.1 mg, 0.2 mmol) were dissolved in THF/H_2O (40 mL/5 mL) under inert atmosphere. The mixture was placed in a 200 mL Schlenk flask and stirred under reflux for 48 h. After cooling to room temperature, the precipitated solids were separated by suction filtration and thoroughly washed with deionized water (50 mL×3), THF (50 mL×3), and MeOH (50 mL×3) to afford yellow products (332.7 mg, yield 76%). ^{1}H NMR (400 MHz, DMSO-d_6): δ = 8.47 (s, 2 H), 8.34-8.27 (q, 4 H); 7.93-7.91 (d, 4 H), 7.56-7.54 (d, 4 H), 4.16 (s, 4 H). MS: calcd for $C_{30}H_{18}N_2O_2$: 438.14, found: 439.14 $[M+H]^+$.

The corresponding ^{1}H NMR and Mass spectra are shown as follows:

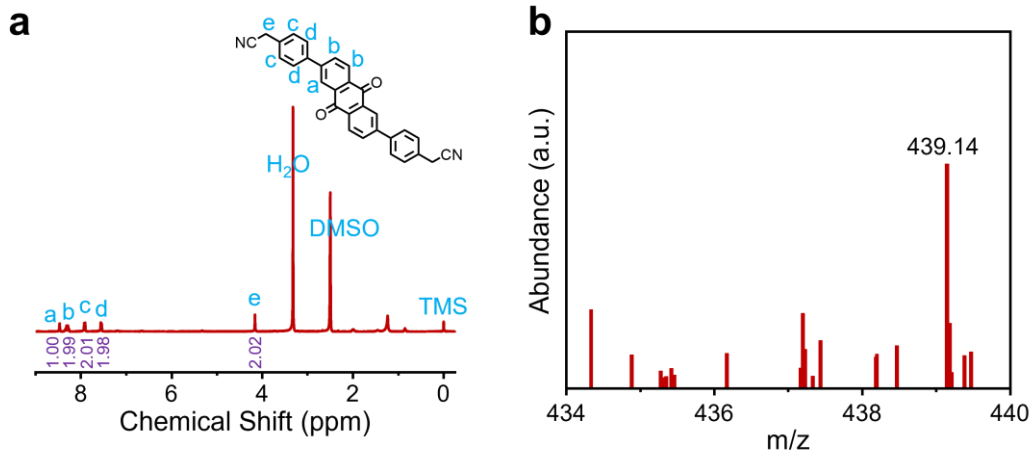

(a) ^{1}H NMR and (b) Mass spectra of AQDAN.

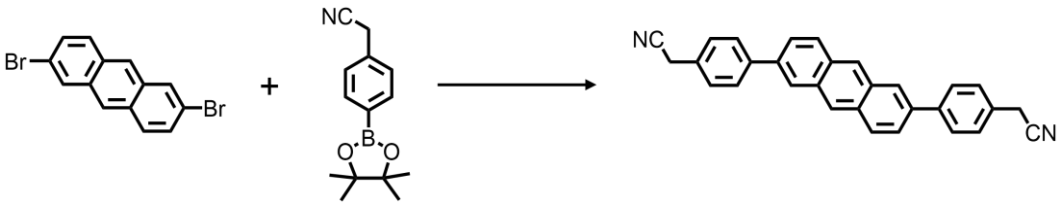

Scheme S2. Synthesis of 2,2'-(anthracene-2,6-diylbis(4,1-phenyl))diacetonitrile (ANDAN).

Synthesis of 2,2'-(anthracene-2,6-diylbis(4,1-phenyl))diacetonitrile (ANDAN): 2,6-dibromoanthracene (336.0 mg, 1 mmol), 4-(cyanomethyl)benzeneboronic acid pinacol ester (607.8 mg, 2.5 mmol),, K_2CO_3 (829.3 mg, 6 mmol), and $Pd(PPh_3)_4$ (231.1 mg, 0.20 mmol) were dissolved in THF/H_2O (40 mL/5 mL) under inert atmosphere. The mixture was placed in a 200 mL Schlenk flask and stirred under reflux for 48 h. After cooling to room temperature, the precipitated solids were separated by suction filtration and thoroughly washed with deionized water (50 mL×3), THF (50 mL×3), and MeOH (50 mL×3) to afford yellow products (293.9 mg, yield 72%). ^{1}H NMR (400 MHz, DMSO-d_6): δ = 8.69 (s, 2 H), 8.42 (s, 2 H); 8.23-8.21 (d, 2 H), 7.94-7.89 (m, 6 H), 7.54-7.51 (d, 4 H), 4.14 (s, 4 H). MS: calcd for $C_{30}H_{20}N_2$: 408.17, found: 409.17 $[M+H]^+$.

The corresponding ^{1}H NMR and Mass spectra are shown as follows:

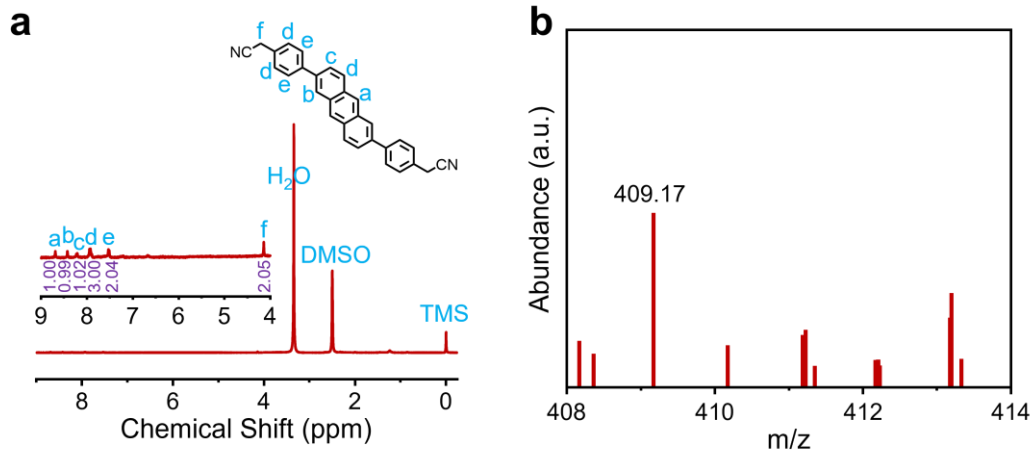

(a) ^{1}H NMR and (b) Mass spectra of ANDAN.

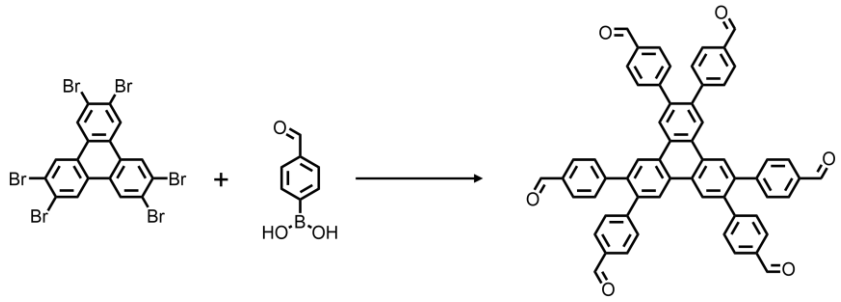

Scheme S3. Synthesis of 2,3,6,7,10,11-hexakis(4-formylphenyl)triphenylene (HFPTP).

Synthesis of 2,3,6,7,10,11-hexakis(4-formylphenyl)triphenylene (HFPTP): 2,3,6,7,10,11-hexabromotriphenylene (701.7 mg, 1 mmol), 4-formylphenylboronic acid (1349.5 mg, 9 mmol), K_2CO_3 (1243.9 mg, 9 mmol), and $Pd(PPh_3)_4$ (693.3 mg, 0.6 mmol) were dissolved in toluene/1,4-dioxane /MeOH (50 mL/25 mL/25 mL) under inert atmosphere. The mixture was placed in a 200 mL Schlenk flask and stirred under reflux for 48 h. After cooling to room temperature, the mixed solvent was removed by evaporation, and the crude product was extracted using dichloromethane and saturated NaCl solution. The organic phase was dried with anhydrous sodium sulfate. After evaporating the solvent, the crude product was purified by column chromatography to afford white crystals (433.9 mg, yield 51%).^{1}H NMR (400 MHz, $CDCl_3$): δ = 10.03 (s, 6H), 8.77 (s, 6H), 7.86-7.84 (d, 12H), 7.51-7.49 (d, 12H). MS: calcd for $C_{60}H_{36}O_6$: 852.25, found: 852.25 $[M]^+$.

The corresponding ^{1}H NMR and Mass spectra are shown as follows:

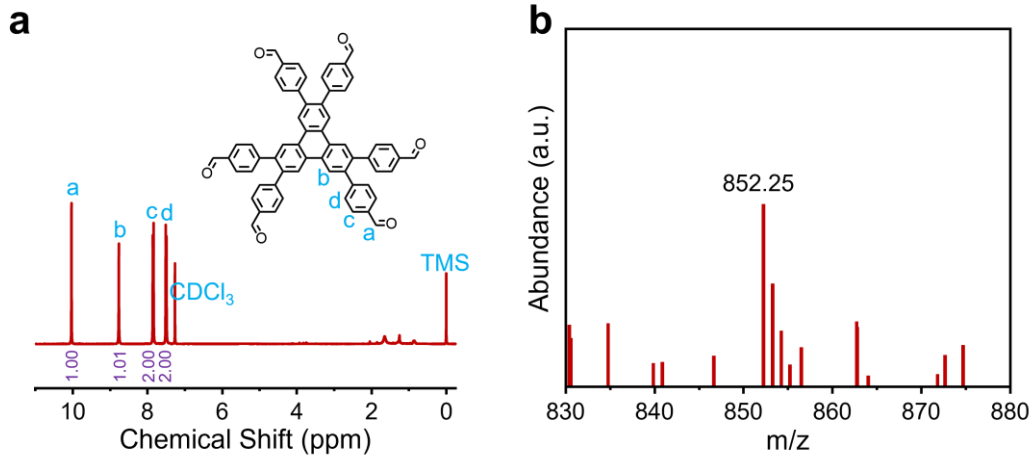

(a) ^{1}H NMR and (b) Mass spectra of HFPTP.

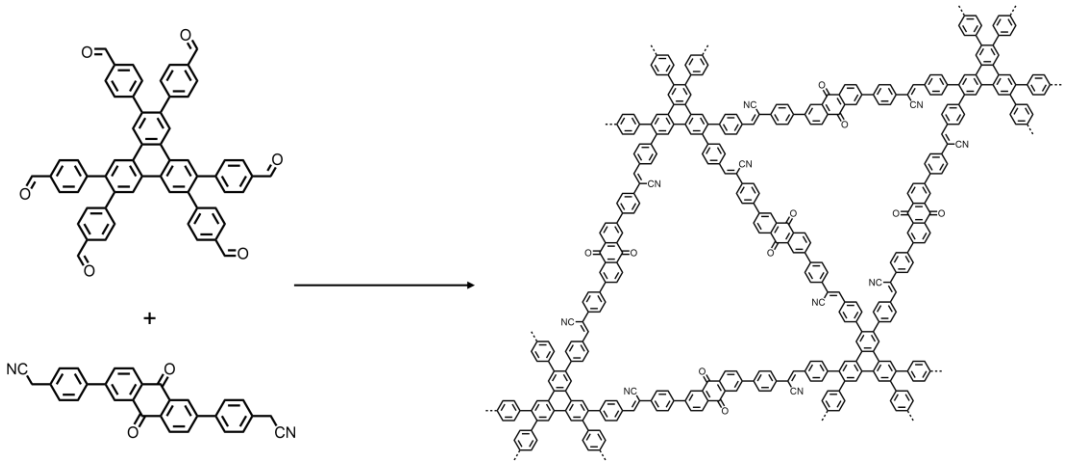

Scheme S4. Synthesis of AQ-HPTP COF.

Synthesis of AQ-HPTP COF: AQDAN (19.7 mg, 0.045 mmol) and HFPTP (12.8 mg, 0.015 mmol) were uniformly dispersed in *o*-DCB/MeOH (1.9 mL/0.1 mL). The dispersion was placed in a 10 mL ampoule and sonicated for 5 min. 0.1 mL TBAH (1.0 M in methanol) and 0.1 mL deionized water were added to the ampoule and sonicated for an additional 5 min. The ampoule was degassed through three freeze-pump-thaw cycles before flame-sealing under vacuum, which was then heated at 120 °C for 3 days. After the reaction was complete, the resulting mixture was cooled to room temperature, and the precipitate was collected by suction filtration, washed with DMF (50 mL×3), deionized water (50 mL×3), acetone (50 mL×3), and THF (50

mL×3). The obtained sample was further purified by Soxhlet extraction with methanol, THF, and dichloromethane, respectively, and dried under vacuum at 80 °C for 12 h to afford the AQ-HPTP COF (26.0 mg, yield 84 %). Anal. Calcd. for $(C_{25}H_{13}NO)_n$: C, 87.4 %; H, 3.8 %; N, 4.1 %; O, 4.7 %; Found: C, 87.1 %; H, 3.7 %; N, 4.2 %; O, 5.0 %.

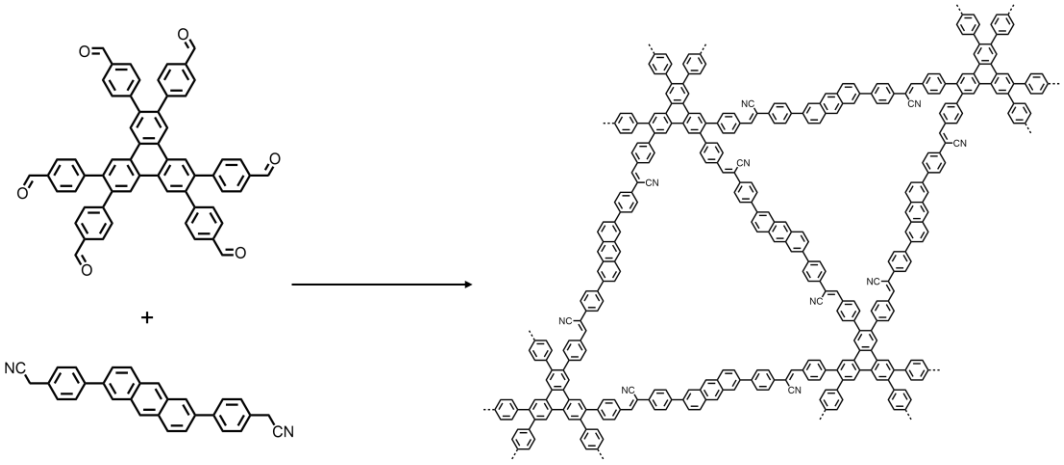

Scheme S5. Synthesis of AN-HPTP COF.

Synthesis of AN-HPTP COF: ANDAN (18.4 mg, 0.045 mmol) and HFPTP (12.8 mg, 0.015 mmol) were uniformly dispersed in *o*-DCB/EtOH (1.8 mL/0.2 mL). The dispersion was placed in a 10 mL ampoule and sonicated for 5 min. 0.1 mL TBAH (1.0 M in methanol) and 0.1 mL deionized water were added to the ampoule and sonicated for an additional 5 min. The ampoule was degassed through three freeze-pump-thaw cycles before flame-sealing under vacuum, which was then heated at 120 °C for 3 days. After the reaction was complete, the resulting mixture was cooled to room temperature, and the precipitate was collected by suction filtration, washed with DMF (50 mL×3), deionized water (50 mL×3), acetone (50 mL×3), and THF (50 mL×3). The obtained sample was further purified by Soxhlet extraction with methanol, THF, and dichloromethane, respectively, and dried under vacuum at 80 °C for 12 h to afford the AN-HPTP COF (23.3 mg, yield 79 %). Anal. Calcd. for $(C_{25}H_{14}N)_n$: C, 91.4 %; H, 4.3 %; N, 4.3 %; Found: C, 91.2 %; H, 4.3 %; N, 4.5 %.

General characterizations

Liquid ^{1}H NMR spectra were recorded on a 400 MHz spectrometer (Bruker ascend 400 MHz NMR spectrometer). Chemical shifts of ^{1}H NMR spectra were reported in parts per million relative to tetramethylsilane (δ=0). The following abbreviations described peak splitting patterns when appropriate: s=singlet, d=doublet, t=triplet, q=quartet, m=multiplet, dd=doublet of doublet. FTIR spectra were recorded on a Thermo-Nicolet 6700 spectrometer between 4000-500 cm^{-1}. Scanning electron microscopy (SEM) was performed on a SU8220 Cold Field Emission Scanning Electron Microscope. Transmission electron microscopy (TEM) was conducted on a JEM-2100F High-Resolution Transmission Electron Microscopy. Samples were placed on carbon-coated copper grids and dried under ambient conditions. Powder X-ray diffraction (PXRD) patterns were obtained using a Japan Rigaku DMax-γA rotation anode X-ray diffractometer equipped with graphite monochromatized Cu Kα radiation (λ=1.54178 Å). Solid state ^{13}C NMR spectra were recorded on a Bruker Avance III 400 MHz NMR spectrometer. Optical diffuse reflectance spectra (DRS) were collected at room temperature with a UV-vis spectrophotometer (DUV-3700, Shimazu). A white standard of $BaSO_4$ was used as a reference. Time-correlated single photon counting (TCSPC) measurements were conducted using a single photon counting controller (Fluorohub, Horiba Scientific) to collect the photoluminescence decay profiles. Thermogravimetric analysis (TGA) was performed from room temperature to 800 °C at a heating rate of 10 °C min^{-1} under N_2 atmosphere using the TA Q5000IR thermalgravimetric analyzer. The nitrogen physisorption experiments were conducted at 77 K on a Micromeritics Tristar II 3020 Surface Area and Pore Analyzer. Structural simulations of AQ-HPTP COF and AN-HPTP COF were performed in the Accelrys Materials Studio software package using the Forcite module. The final lattice parameters and the refined PXRD patterns were obtained until the values of R_{wp} and R_p converged.

Synchrotron radiation photoemission spectroscopy (SRPES) measurements: The measurements were conducted to determine the valence band (VB) positions of COFs. SRPES experiments were performed at the Catalysis and Surface Science Endstation (BL11U) in the National Synchrotron Radiation Laboratory (NSRL) in Hefei, China. An excitation of 50.0 eV was utilized to obtain the secondary electron cutoff. The binding energy (BE) was calibrated and referenced to the Fermi level (E_F) of a gold foil. The work function (W_F) of samples was determined according to equation $\Phi = h\nu - \Delta E$, where is ΔE the spectrum width, i.e. the energy difference between the secondary electron cutoff and the E_F of tested sample. To obtain the secondary electron cutoff, a -5 V bias was applied to the sample, which accelerated all the photoelectrons with higher kinetic energy (KE) to overcome the W_F of analyzer.

In situ diffuse reflectance infrared Fourier transform spectroscopy (DRIFTS) measurements: In situ DRIFTS measurements were performed using a Bruker INVENIO-S Fourier transform spectrometer equipped with a SharpX diffuse reflectance accessory. Each spectrum was recorded by averaging 100 scans at a 4 cm^{-1} spectral resolution. The samples were held in a custom-made IR reaction chamber which was specifically designed to examine highly scattering powder samples in the diffuse reflection mode. The chamber was sealed with two BaF_2 windows.

Photoelectrochemical and electrochemical measurements: All the measurements were conducted on a Metrohm Autolab PGSTAT302N potentiostat/galvanostat in a three-electrode cell system. A standard three-electrode setup was used with the Pt-wire and Ag/AgCl (saturated KCl) as counter and reference electrodes, respectively. The illumination source is a 300 W Xe lamp (Perfect Light PLS-SXE 300).

Photocatalytic H_2O_2 production tests: 20 mg COFs and 10 mL deionized water were put in an unsealed device mainly composed of a quartz tube and gas flow components. The suspension was well dispersed by sonication for 30 min. Prior to the photocatalytic test, the air in the device

was removed and O_2 was bubbled into the suspension for 30 min in the dark. In order to reach the adsorption-desorption equilibrium, the suspension was further stirred in the dark for 30 min. A 300 W Xe lamp (Perfect Light PLS-SXE 300) was used as the light source, and O_2 was continuously bubbled into the device. A cutoff filter (Kenko L-42) was used to achieve visible light irradiation (λ>420 nm, average intensity: 100 mW cm^{-2}). The concentration of H_2O_2 was determined by UV-vis spectrophotometer. For example, 1 mL suspension was sampled and centrifuged at 14000 rpm and then filtrated with a 0.22 μm filter to further remove the photocatalysts. The sample was mixed with pre-prepared $Ce(SO_4)_2$ solution. The concentrations of H_2O_2 were determined by the UV-vis spectrophotometer.

Determination of H_2O_2 concentration: The H_2O_2 concentration was measured by a cerium sulfate $Ce(SO_4)_2$ titration method, which was the same as our previous work[1].

Recycling tests: After each 4-hour photocatalytic reaction, the suspension was centrifuged to separate the photocatalyst from the solution. The recovered photocatalyst was then thoroughly washed with deionized water (20 mL×3) to remove any residual species, followed by vacuum drying at 80°C for 12 hours. Once dried, the photocatalyst was weighed and reused in the subsequent cycle to ensure consistency in each cycle.

Photocatalytic decomposition of H_2O_2 over COFs: The decomposition of H_2O_2 was conducted by suspending catalysts (50 mg) in aqueous solution (100 mL) containing H_2O_2 (1 mM) under the Ar atmosphere. A 300 W Xe lamp (Perfect Light PLS-SEX 300) was used as the light source. A cutoff filter (Kenko L-42) was used to achieve visible-light irradiation (λ>420 nm, average intensity: 100 mW cm^{-2}).

SCC efficiency measurements: The solar-to-chemical energy conversion (SCC) efficiency was determined by using an AM 1.5G solar simulator as the light source (average intensity: 100 mW cm^{-2}). Photocatalysts (600 mg) and water (100 mL) were put in an unsealed device mainly composed of a quartz tube and gas flow components. During the photocatalytic tests, O_2 was

continually bubbled into the bottle, and λ>420 nm cutoff filter was used to inhibit the decomposition of the formed H_2O_2 by UV light.

The SCC efficiency was calculated via following equation (1):

$$\text{SCC efficiency}(\%)=\frac{[\Delta G \text{ for } H_2O_2 \text{ generation (J mol}^{-1})][H_2O_2 \text{ formed (mol)}]}{[\text{Total input power (W)}][\text{Reaction time (s)}]}\times 100\% \quad (1)$$

Where ΔG= 117 kJ mol^{-1}.

For example, when using AQ-HPTP COF as the photocatalyst, the irradiated sample areas are 4.0 cm^2 during 1 h of illumination. Therefore, the calculated total input energy (J) is 1440 J. During the photocatalytic reaction, 259.0 μmol H_2O_2 was generated and the energy generated by photocatalytic H_2O_2 production is 30.30 J. Consequently, the SCC efficiency can be calculated as equation (2):

$$\text{SCC efficiency }(\%)=\frac{30.30 \text{ J}}{1440 \text{ J}}\times 100\%=2.10\% \quad (2)$$

Apparent quantum efficiency (AQE) measurements: The AQE for H_2O_2 evolution was measured under the illumination of a 300 W Xe lamp with different bandpass filters (central wavelength λ_0, FWHM=20 nm) for 1 h. The reported AQE values here are the maximum attainable results after varying the amounts of photocatalysts used, the light intensity, and the light absorption areas. The AQEs were calculated using the following equation (3):

$$\text{AQE }(\%)=\frac{\text{Number of reacted electrons}}{\text{Number of incident electrons}}\times 100\%$$

$$=\frac{2\times\text{Number of evolved } H_2O_2 \text{ molecules}}{\text{Number of incident electrons}}\times 100\% \quad (3)$$

For example, at λ_0=420 nm for AQ-HPTP COF, the average intensity of irradiation was determined to be 10.0 mW cm^{-2} by an ILT 950 spectroradiometer, and the irradiation area was controlled at 4.0 cm^2. The number of incident photons (N) is 5.05×10^{-4} (equation (4)).

$$N\ (mol)=\frac{E}{h\nu}=\frac{10.0\times10^{-3}\times4\times1\times3600\times420\times10^{-9}}{6.626\times10^{-34}\times3\times10^{8}\times6.022\times10^{23}}=5.05\times10^{-4}\ mol \quad (4)$$

The amount of H_2O_2 molecules generated in 1 hour was 65.0 μmol. Thus the AQE calculated from the above equation is 25.74 % (equation (5)).

$$AQE\ (\%)=\frac{2\times65.0\times10^{-6}}{5.05\times10^{-4}}\times100\%=25.74\% \quad (5)$$

Continuous-flow photocatalytic reactor: The continuous-flow photocatalytic reactor consisted of a deionized water container, an air pump, a peristaltic pump, a flow reactor, a 300 W Xe lamp (Perfect Light PLS-SXE 300), and an H_2O_2 container. The flow reactor was made of quartz and contained nine microreactors, each with a diameter of 12 mm and a depth of 10 mm. These microreactors were connected by channels that are 2 mm wide and 2 mm deep. AQ-HPTP COF was sonically dispersed in water to form a slurry, which was then uniformly filled into the microreactors, with cotton filling the channels between them. In addition, each microreactor was equipped with a miniature magnetic stirrer to ensure a uniform suspension. Air-saturated water was pumped into the flow reactor at a rate of 1 mL min^{-1}. A cutoff filter (Kenko L-42) was used to achieve visible-light irradiation (>420 nm). This continuous-flow photocatalytic reactor enables the continuous H_2O_2 production under illumination.

Photocatalytic hydrogen evolution tests: 20 mg photocatalysts and 10 mL deionized water (containing 10% MeOH as a hole scavenger) were put in a hermetic device mainly composed of a quartz tube and sealing components. The suspension was well dispersed by ultrasonication for 30 min, and Ar was bubbled into the suspension for 30 min in the dark. A 300 W Xe lamp (Perfect Light PLS-SXE 300) was used as the light source. A cutoff filter (Kenko L-42) was used to achieve visible-light irradiation (>420 nm, average intensity: 100 mW cm^{-2}). The amount of H_2 evolved was determined using gas chromatography (SHIMADZU GC-2014, thermal conductivity detector (TCD), Ar carrier, Agilent).

Photocatalytic water oxidization tests: 20 mg photocatalysts and 10 mL deionized water (containing 0.01 M $NaIO_3$ as electron acceptor and 0.1 g La_2O_3 as a pH buffer agent) were put in a hermetic device mainly composed of a quartz tube and sealing components. The suspension was well dispersed by ultrasonication for 30 min. Before the photocatalytic test, the air in the device was removed by purging with Ar flow for 30 min in the dark. A 300 W Xe lamp (Perfect Light PLS-SXE 300) was used as the light source. A cutoff filter (Kenko L-42) was used to achieve visible-light irradiation (>420 nm, average intensity: 100 mW cm^{-2}). The amount of O_2 evolved was measured by both NeoFox Sport Oxygen Sensor (Ocean Optics) and gas chromatography (SHIMADZU GC-2014, thermal conductivity detector (TCD), Ar carrier, Agilent). The amount of H_2O_2 evolved was measured by the UV-vis spectrophotometer.

Isotope labeling experiments: 4 mg photocatalysts and 2 mL $H_2{}^{18}O$ (99%) were put in a hermetic device mainly composed of a quartz tube and sealing components. The suspension was well dispersed by sonication for 30 min. After O_2 was bubbled into the suspension for 20 min in the dark, the suspension was stirred for 30 min in the dark to reach the absorption-desorption equilibrium. The quartz tube was then irradiated using a 300 W Xe lamp. A cutoff filter (Kenko L-42) was employed to achieve visible light (λ>420 nm) irradiation. After 1 h irradiation, the gas products in the headspace of the reaction vessel were analyzed by GC-MS (Thermo Fisher GC ULTRA/ISQ MS).

Meanwhile, the formed H_2O_2 was decomposed by catalase enzyme under Ar atmosphere (equation (6)):

$$2H_2O_2 \xrightarrow[\text{Ar}]{\text{catalase enzyme}} 2H_2O+O_2 \quad (6)$$

Hence, the O_2 generated by the decomposition of photogenerated H_2O_2 was analyzed by GC-MS.

Hall effect measurements: Hall effect measurements were conducted using the Semishare X3 Hall Effect Test System, equipped with a PPMS-9 platform for precise temperature and magnetic field control, a KEITHLEY 2400 Source Meter, and a KEITHLEY 2182A Nanovoltmeter. At room temperature, 20 mg of COFs were placed in a press mold, compressed under a pressure of 10 MPa, and held for 4 h. The resulting compressed pellet samples were measured 8 mm in diameter and 0.4 mm in thickness. The silver paste was meticulously applied to each of the four corners of the samples (0.2 cm × 0.2 cm). Conductivity and mobility assessments were performed using van der Pauw geometry under both vacuum and ambient air conditions. Electrode probes constructed of needle-point gold-plated copper were used, with an external voltage of 1 V applied for the Hall effect measurements. The current-voltage curves were analyzed to ensure ohmic contacts at all connections. Data were collected and processed using a LabVIEW-based programming system.

Electron paramagnetic resonance (EPR) measurements: Spin trapping-EPR tests were recorded using a JEOL JES-FA 200 model spectrometer operating at the X-band frequency (9.4 GHz). 5,5-dimethyl-1-pyrroline N-oxide (DMPO) was used as a spin-trapping reagent to detect •OH or $\bullet O_2^-$. The measurements were conducted as follows: photocatalysts (2 mg) were dispersed in $NaIO_3$ aqueous solutions (0.01 M, 500 μL) or a MeOH/water mixture (9/1 v/v, 500 μL) containing DMPO (0.1 mmol) with a Pyrex glass tube which was sealed with a rubber septum cap. A 300 W Xe lamp was used as the light source. The dispersion was purged with Ar or O_2 gas for 5 min before light irradiation.

Rotating disk electrode (RDE) measurements: A glassy carbon rotating disk electrode (PINE Research Instrumentation, USA) served as the substrate for the working electrode. The working electrode was prepared as follows: COFs (4 mg) were dispersed in EtOH (2 mL) containing Nafion (40 μL) by ultrasonication. The slurry (20 μL) was put onto the disk electrode and dried at room temperature. The linear sweep voltammograms (LSV) were obtained in an O_2-saturated

0.1 M phosphate buffer solution (pH=7) at room temperature with a scan rate of 10 mV/S and different rotation speeds after O_2 bubbling for 1 hour. During the reaction, the light source from the Xe-lamp (Perfect Light PLS-SXE 300, average intensity:100 mW cm^{-2}) vertically illuminated at the rotating electrode, where the photoelectrochemical kinetic information and the formation of peroxide could be obtained. The average number of electrons (n) was calculated by Koutecky-Levich equation (7) and (8):

$$\frac{1}{J} = \frac{1}{J_L} + \frac{1}{J_K} = \frac{1}{B\omega^{\frac{1}{2}}} + \frac{1}{J_K} \quad (7)$$

$$B = 0.62nFC_0D_0^{\frac{2}{3}}\nu^{-\frac{1}{6}} \quad (8)$$

where J is the measured current density, J_K and J_L are the kinetic and diffusion-limiting current densities, ω is the angular velocity, n is transferred electron number, F is Faraday constant (96485 C mol^{-1}), C_0 is the bulk concentration of O_2 (1.26×10^{-6} mol cm^{-3}), D_0 is the diffusion coefficient of O_2 in 0.1 M phosphate buffer solution (2.7×10^{-5} cm^2 s^{-1}), and ν is kinetic viscosity of the electrolyte (0.01 cm^2 s^{-1}), respectively.

Rotating ring-disk electrode (RRDE) measurements: A ring-disk electrode (PINE Research Instrumentation, USA) served as the substrate for the working electrode. The working electrode was prepared as RDE measurements. RRDE measurements were conducted on a rotating-ring disk system under 300 W Xe lamp (Perfect Light PLS-SXE 300, average intensity:100 mW cm^{-2}) light illumination. The voltammograms were obtained in a 0.1 M phosphate buffer solution (pH=7) at room temperature under an Ar atmosphere with a scan rate of 10 mV s^{-1} and a rotation rate of 1000 rpm. The phosphate buffer solution electrolyte was purged with Ar for 1 h prior to the measurements. During the reaction, a light source from the Xe-lamp vertically illuminated the rotating electrode, where the photoelectrochemical kinetic information and the formation of peroxide could be obtained. The potential of the ring electrode was set to -0.3 and 0.6 V (vs. Ag/AgCl) to detect O_2 or H_2O_2, respectively.

Computational Details: All calculations of molecular models in this study were performed with the Gaussian 16 package. B3LYP functional and the 6–31 G (d, p) basis set were employed to calculate structure. The simulation of periodic COF structure was carried out using density functional theory (DFT) methods within the Vienna Ab-initio Simulation Package (VASP),[2,3] with the Perdew-Burke-Ernzerhof exchange-correlation functional.[4] The Brillouin zones were sampled with 3 × 3 × 1 Γ-centered k-points. The projector augmented wave (PAW)[3,5] method was employed to describe electron-ion interactions, with a plane wave energy cutoff set at 500 eV. Exchange-correlation interactions were addressed using the generalized gradient approximation (GGA) as formulated by Perdew, Burke, and Ernzerhof (PBE).[6] The hybrid functional of HSE06, which combines HF exchange with the exchanges of PBE exchange-correlation functional, was employed for the calculation of electronic structure.[7] The convergence criterion for interatomic forces during optimization was set to 0.02 eV $Å^{-1}$, and the total energy convergence criterion for wave function self-consistency was set to 10^{-5} eV. A vacuum region of about 20 Å was used to eliminate the interaction of layers for layers in all structures. The electronic band calculations were performed with DFT by combining the VASP with the post-processing VASPKIT package.[8] The free energy change (ΔG) during ORR and WOR on the surface of 2D COFs was calculated based on the computational hydrogen electrode (CHE) model developed by Nørskov et al.[9]

On the COF mentioned in this article, the WOR process could be decomposed into four one-electron oxidation steps, corresponding to the deprotonation of water molecules, as follows:

Step1: $* + H_2O \rightarrow *OH + H^+ + e^-$

Step2: $*OH \rightarrow *O* + H^+ + e^-$

Step3: $*O* + H_2O \rightarrow *O*OH + H^+ + e^-$

Step4: $*O*OH \rightarrow *OO* + H^+ + e^-$

Step5: $*OO* \rightarrow * + O_2$

As for ORR, the reaction mechanism is as follows:

Step6: $* + O_2 \rightarrow *OO$

Step7: $*OO + 2H^+ + 2e^- \rightarrow *HOOH$

Step8: $*HOOH \rightarrow * + H_2O_2$

Specially, for ORR in AQ moiety, the reaction mechanism is as follows:

Step9: $* + 2H^+ + 2e^- \rightarrow *H*H$

Step10: $*H*H + O_2 \rightarrow * + H_2O_2$

where * denotes the site on the surface, and * (radical) denotes the corresponding radical adsorbed on the surface.

Gibbs free energy calculations were conducted to determine the Gibbs free energy changes (ΔG) for each reaction step. The ΔG values were obtained using the formula: $G(T) = E + H(T) - TS(T)$, where E denoted the self-consistent field energy for the given species. The $H(T)$ or $S(T)$ were calculated by accounting for all relevant finite temperature effects, including vibration, rotation, and translation for gas-phase species. For adsorbed species, only the vibration contributions of the fixed materials were considered, as rotational and translational motions were restricted.

Table S1. Summary of R^2, FWHM, and crystalline domain sizes of AQ-HPTP COF and AN-HPTP COF.

Photocatalyst	R^2	FWHM[a)]	Crystalline domain sizes (nm)[b)]
AQ-HPTP COF	0.980	0.221	35.92
AN-HPTP COF	0.989	0.254	31.30

[a)] The full width at half maximum (FWHM) were obtained from Supporting Information Figure S2 using Lorenz function.

[b)] The crystalline domain sizes were calculated by Scherrer equation as follow:

$$\text{Crystalline domain size (nm)} = \frac{K\gamma}{\beta\cos(\theta)}$$

where K is the the shape factor, γ is the wavelength of the incident X-ray, β is the FWHM which is the width at which the diffracted intensity is half the maximum (the unit is expressed in radians), θ is the Bragg angle.

Table S2. Summary of recently reported SCC efficiencies of COFs for photocatalytic H_2O_2 production.

Photocatalyst	Conditions	SCC Efficiency (%)	Ref.
TB-COF	water, white LED 17 mW cm^{-2}	1.08	*ACS Catal.* **2024**, *14*, 4728–4737
Kf-AQ	water (pH 13), visible light	0.7	*Nat. Commun.* **2024**, *15*, 2649
TBD-COF	water, white LED 17 mW cm^{-2}	1.04	*Angew. Chem. Int. Ed.* **2024**, *63*, e202405763
TP-$DPBD_{3O}$-COF	water, AM 1.5G 100 mW cm^{-2}	0.91	*Nat. Synth.* **2024**, *3*, 998–1010
QP-HPTP-COF	water, AM 1.5G (>420 nm) 100 mW cm^{-2}	1.41	*Adv. Mater.* **2025**, *37*, 2410247
TACOF-1-COOH	water, Xe lamp 140 mW cm^{-2}	0.55	*Angew. Chem. Int. Ed.* **2024**, *63*, e202408802
TAH-COF	water, AM 1.5G 100 mW cm^{-2}	0.66	*J. Am. Chem. Soc.* **2024**, *146*, 20107–20115
TAPT–FTPB COFs	water, AM 1.5G 100 mW cm^{-2}	1.22	*Nat. Synth.* **2025**, *4*, 134–141
EBBT-COF	water, >400 nm 130.2 mW cm^{-2}	1.17	*Adv. Energy Mater.* ***2025***, *15*, *2404497*
COF-JLU90	water, AM 1.5G 100 mW cm^{-2}	1.52	*Angew. Chem. Int. Ed.* **2025**, *64*, e202505286
I-COFs	water, simulated solar 100 mW cm^{-2}	1.88	*Matter*. **2025**, *8*, 102076
BYTT-COF	water, AM 1.5G 100 mW cm^{-2}	1.02	*ACS Catal*. **2025**, *15*, 12541-12550
β-TT-TDAN COF	water, AM 1.5G 100 mW cm^{-2}	1.35	*Adv. Mater.* **2025**, *37*, 2500913
COF-BD2	water, Xe lamp 100 mW cm^{-2}	0.68	*Angew. Chem. Int. Ed.* **2025**, *64*, e202505621
TpPm	water, AM 1.5G 100 mW cm^{-2}	1.84	*Nat Commun.* **2025**, *16*, 6943
COF-S-OH	water, AM 1.5G 100 mW cm^{-2}	2.1	*Angew. Chem. Int. Ed.* **2025**, *64*, e202511024
twist-PmTp-COF	water, AM 1.5G 100 mW cm^{-2}	1.25	*Adv. Mater.* **2025**, doi: 10.1002/adma.202511092
TpPa/TpDz	water, Xe Lamp	1.34	*Nat. Synth.* **2025**, *4*, 1610–1620
HPTP-Ph-COF	water, AM 1.5G 100 mW cm^{-2}	1.06	*Nat Commun.* **2025**, *16*, 6495
AQ-HPTP COF	water, AM 1.5G (>420 nm) 100 mW cm^{-2}, 298 K	2.10	**This work**

Table S3. Summary of recently reported SCC efficiencies of anthraquinone-containing materials for photocatalytic H_2O_2 production.

Photocatalyst	Conditions	SCC Efficiency (%)	Ref.
Kf-AQ	water (pH 13), visible light	0.7	*Nat. Commun.* **2024**, *15*, 2649
DQTb-COFs	water, AM 1.5G	0.21	*Chem. Eng. J.*, **2024**, *481*, 148494
TPT-alkynyl-AQ	water, AM 1.5G 100 mW cm^{-2}	0.35	*Proc. Natl. Acad. Sci. U.S.A.* **22**, 119, e2202913119
PAF-379	water, >420 nm 100 mW cm^{-2}	0.57	*Angew. Chem. Int. Ed.* **2025**, *64*, e202502943
CZ-AQ	water, AM 1.5G 100 mW cm^{-2}	1.25	*Adv. Mater*. **2026**, *38*, e07961
BDP-AAQ	AM 1.5G 100 mW cm^{-2}	0.61	*Angew. Chem. Int. Ed.* **2025**, *64*, e202425017
RF-DHAQ-2	water, AM 1.5G 100 mW cm^{-2}	1.2	*Angew. Chem. Int. Ed.* **2023**, *62*, e202218318
sp^3-SF-AQ	water, AM 1.5G 100 mW cm^{-2}	1.15	*Adv. Funct. Mater.* **2026**, *36*, e19832
TPC-3D	lake water, AM 1.5G 100 mW cm^{-2}	3.6	*Nat Commun.* **2024**, *15*, 5406
O-PTAQ	water, AM 1.5G 100 mW cm^{-2}	1.64	*Adv. Sci.* **2025**, *12*, e03929
ACP	water, 100 mW cm^{-2}	1.92	*J. Mater. Chem. A*, **2024**, *12*, 18433-18439
AQ-HPTP COF	water, AM 1.5G (>420 nm) 100 mW cm^{-2}, 298 K	2.10	**This work**

Table S4. Summary of recently reported H_2O_2 concentration of COFs for continuous-flow photocatalytic H_2O_2 production.

Photocatalyst	**Conditions**	**H_2O_2 concentration (mM)**	**Ref.**
TP-DPBD$_{3O}$-COF	Air+water	0.16	*Nat. Synth.* **2024**, *3*, 998–1010
Hz-TP-BT-COF	Air+water	0.2	*Nat. Catal.* **2024**, *7*, 195–206
TAPT–FTPB COFs	O_2+water	~0.09	*Nat. Synth.* **2025**, *4*, 134–141
I-COFs	Air+water	~1	*Matter*. **2025**, *8*, 102076
COF-BD2	water	~0.3	*Angew. Chem. Int. Ed.* **2025**, *64*, e202505621
TBA-COF	Air+real seawater	~0.8	*Adv. Funct. Mater*. **2025**, *35*, 2421514
PAQ-TABPB	O_2+water	1.04	*Angew. Chem. Int. Ed.* **2025**, *64*, e202508690
ACOF-S-EtOH	Air+water	0.56	*J. Am. Chem. Soc.* **2025**, *147*, 34681–34689
TpPm	water	1.6	*Nat Commun*. **2025**, *16*, 6943
COF-S-OH	water	~0.6	*Angew. Chem. Int. Ed.* **2025**, *64*, e202511024
COF-M180	Air+water	1.75	*Angew. Chem. Int. Ed.* **2025**, *64*, e202519513
AQ-HPTP COF	Air+water	2.4	**This work**

Table S5. The calculated O_2 adsorption energy at different potential adsorption sites for AQ-HPTP COF.

Active sites	**E_{adsorb} (eV)**
triphenylene moiety	0.987
“1” benzene	1.054
vinylene linkage	0.202
cyano moiety	1.107
AQ moiety	1.141
AQH_2	-0.397
“2” benzene	1.047

Table S6. The calculated O_2 adsorption energy at different potential adsorption sites for AN-HPTP COF.

Active sites	**E_{adsorb} (eV)**
triphenylene moiety	0.515
“1” benzene	0.744
vinylene linkage	-0.056
cyano moiety	1.020
AN moiety	0.256
“2” benzene	0.483

Table S7. The calculated Gibbs free energy changes (ΔG) for the formation of *OH at different potential active sites toward the four-electron WOR on AQ-HPTP COF. U_{ox}=2.297 eV is the potential caused by photogenerated holes for the four-electron WOR.

Active sites	**ΔG (eV)**	**ΔG-U_{ox} (eV)**
triphenylene moiety	2.074	-0.223
“1” benzene	2.119	-0.178
vinylene linkage	2.035	-0.262
cyano moiety	2.518	0.221
AQ moiety	2.719	0.422
“2” benzene	2.346	0.049

Table S8. The calculated Gibbs free energy changes (ΔG) for the formation of *OH at different potential active sites toward the four-electron WOR on AN-HPTP COF. U_{ox}=1.974 eV is the potential caused by photogenerated holes for the four-electron WOR.

Active sites	**ΔG (eV)**	**ΔG-U_{ox} (eV)**
triphenylene moiety	2.136	0.162
“1” benzene	2.279	0.305
vinylene linkage	1.389	-0.585
cyano moiety	2.061	0.087
AN moiety	1.652	-0.322
“2” benzene	2.275	0.301

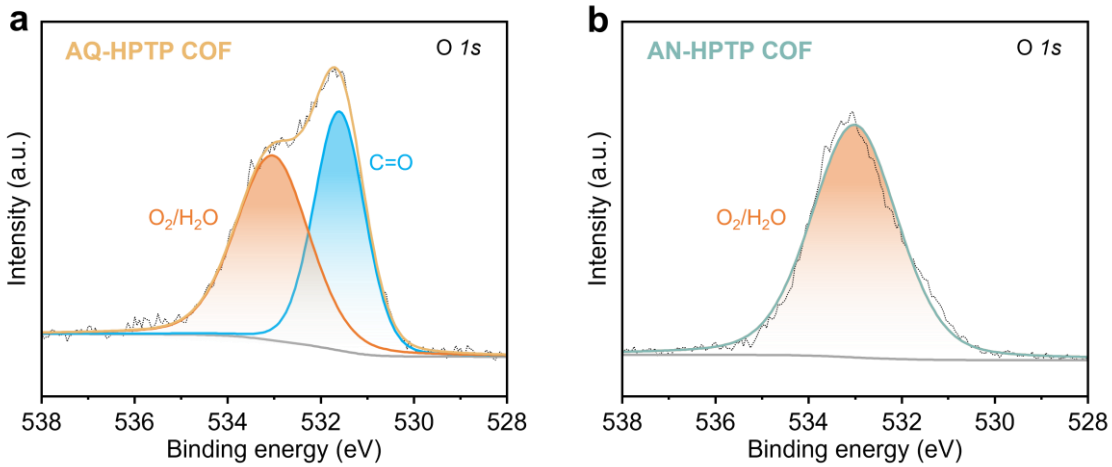

Figure S1. High-resolution O *1s* XPS spectra of (a) AQ-HPTP COF and (b) AN-HPTP COF.

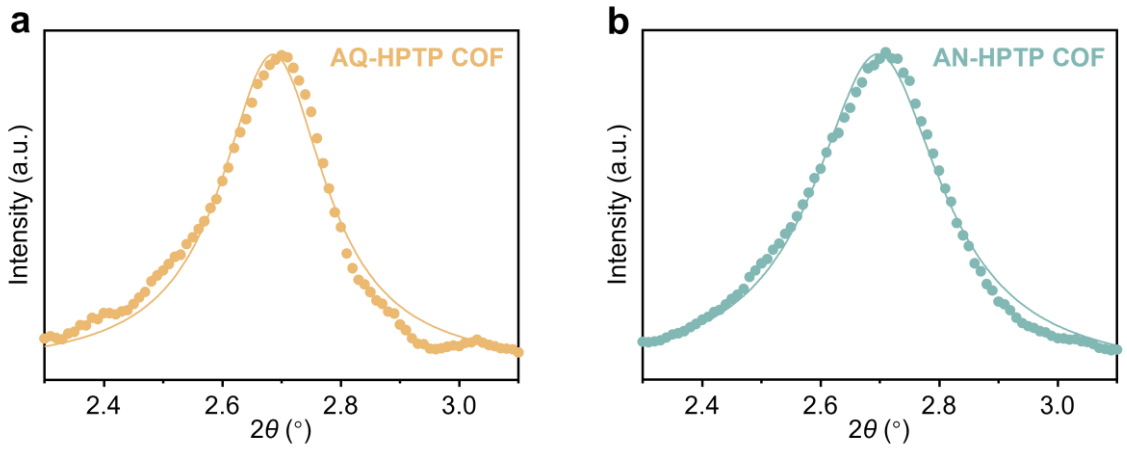

Figure S2. The (100) X-ray diffraction peaks with fitted results obtained by Lorenz function and corresponding crystalline domain sizes of (a) AQ-HPTP COF and (b) AN-HPTP COF.

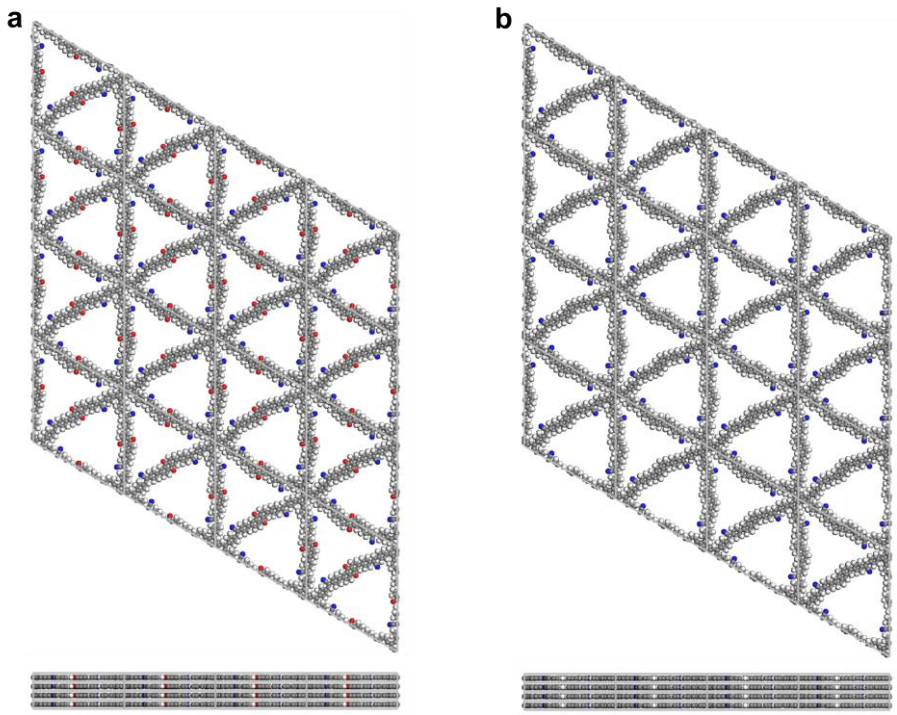

Figure S3. The reconstructed lattice structure of (a) AQ-HPTP COF and (b) AN-HPTP COF via the simulated AA stacking model.

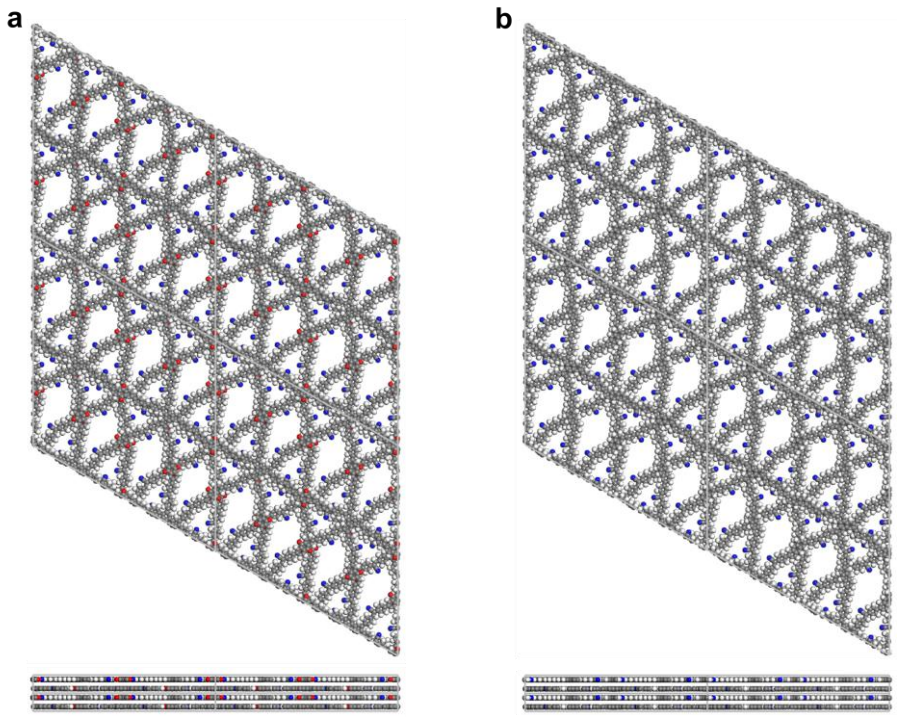

Figure S4. The reconstructed lattice structure of (a) AQ-HPTP COF and (b) AN-HPTP COF via the simulated AB stacking model.

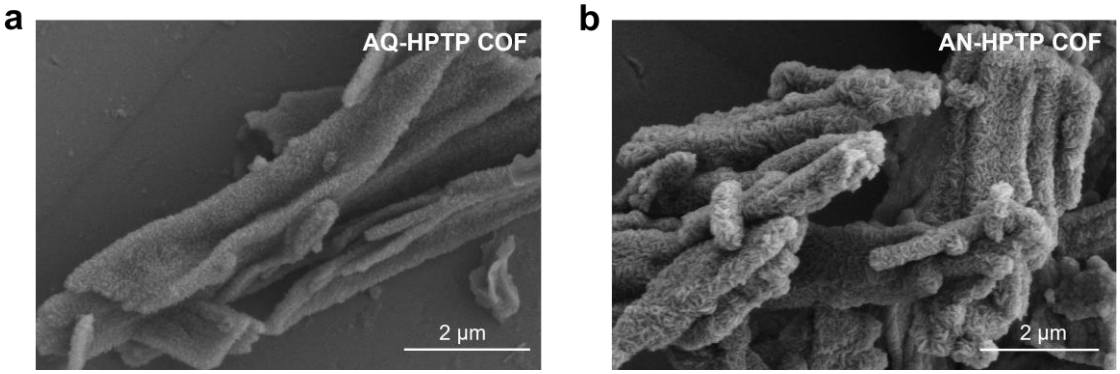

Figure S5. SEM images of (a) AQ-HPTP COF and (b) AN-HPTP COF.

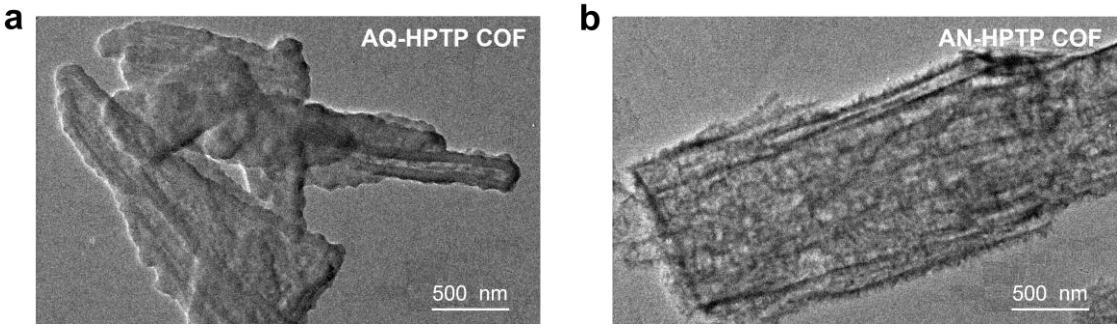

Figure S6. TEM images of (a) AQ-HPTP COF and (b) AN-HPTP COF.

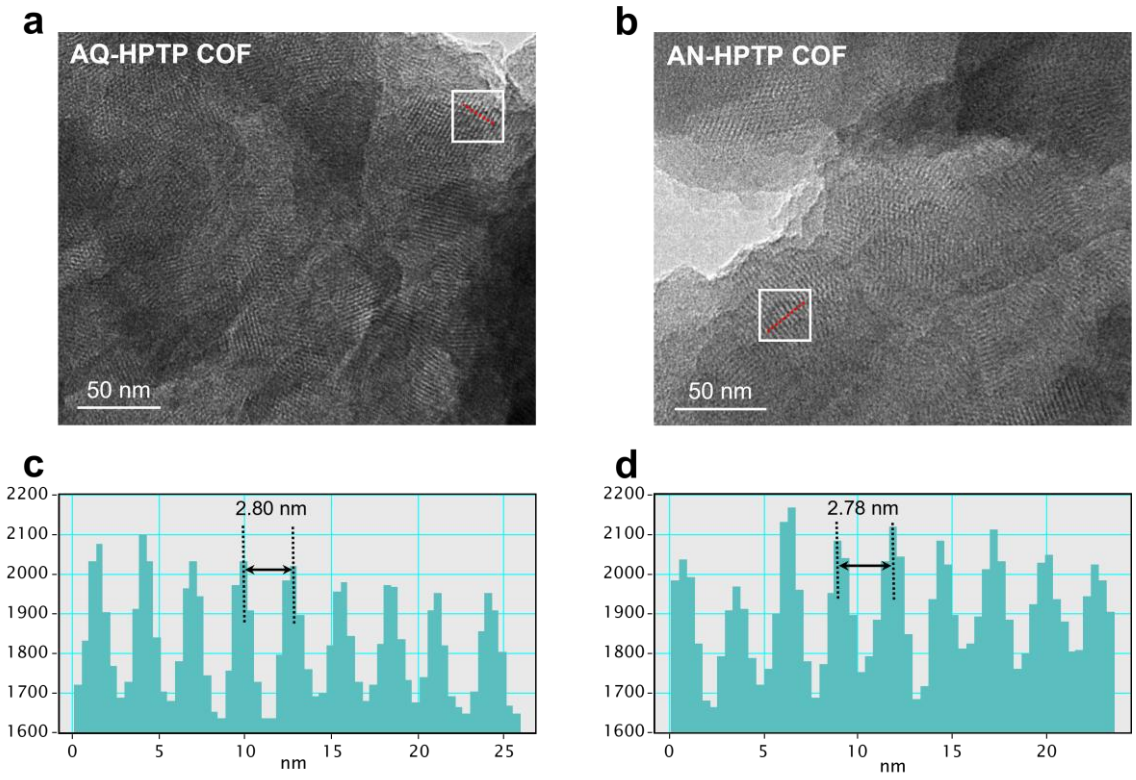

Figure S7. High-resolution TEM images of (a) AQ-HPTP COF and (b) AN-HPTP COF. Corresponding statistical line intensity profile of lattice planes of (c) AQ-HPTP COF and (d) AN-HPTP COF analyzed using the Digital Micrograph software.

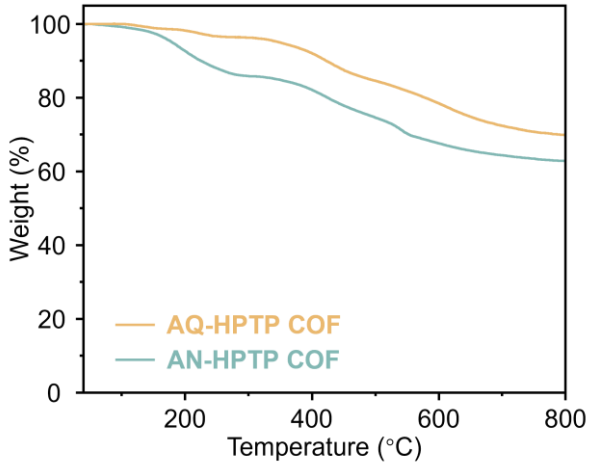

Figure S8. TGA profiles of AQ-HPTP COF and AN-HPTP COF measured at a heating rate of 10 °C/min under an N_2 atmosphere.

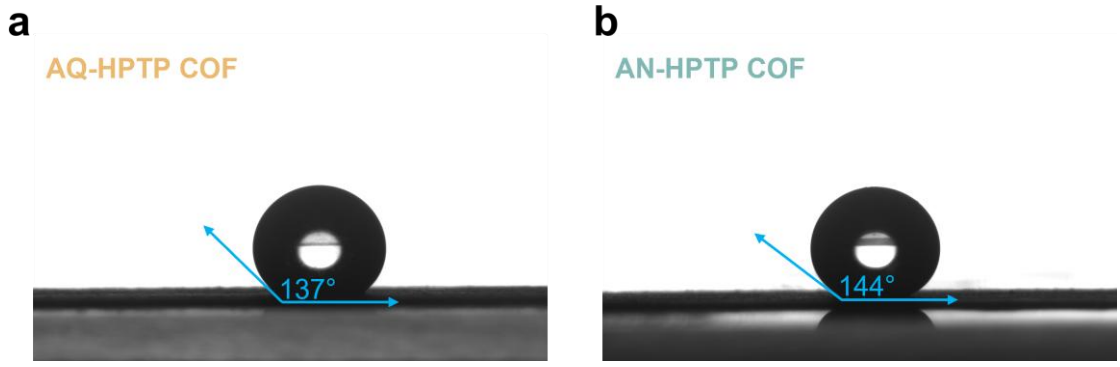

Figure S9. Water contact angles for (a) AQ-HPTP COF and (b) AN-HPTP COF.

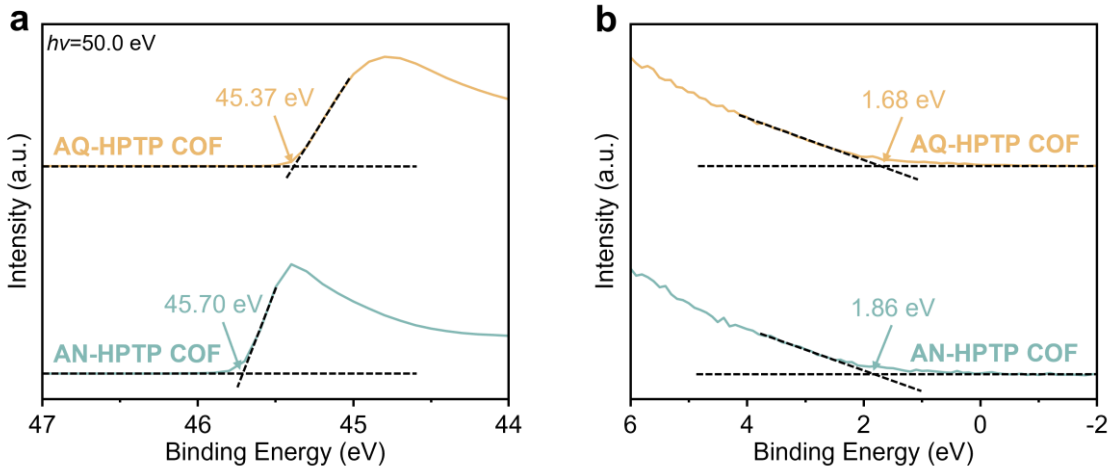

Figure S10. (a) Secondary electron cut-off and (b) valence band spectra of both COFs. The work functions (Φ) of AQ-HPTP COF and AN-HPTP COF are calculated to be -4.63 and -4.30 eV, respectively. Meanwhile, the VB positions of AQ-HPTP COF and AN-HPTP COF are 1.68 and 1.86 eV below the E_F, respectively.

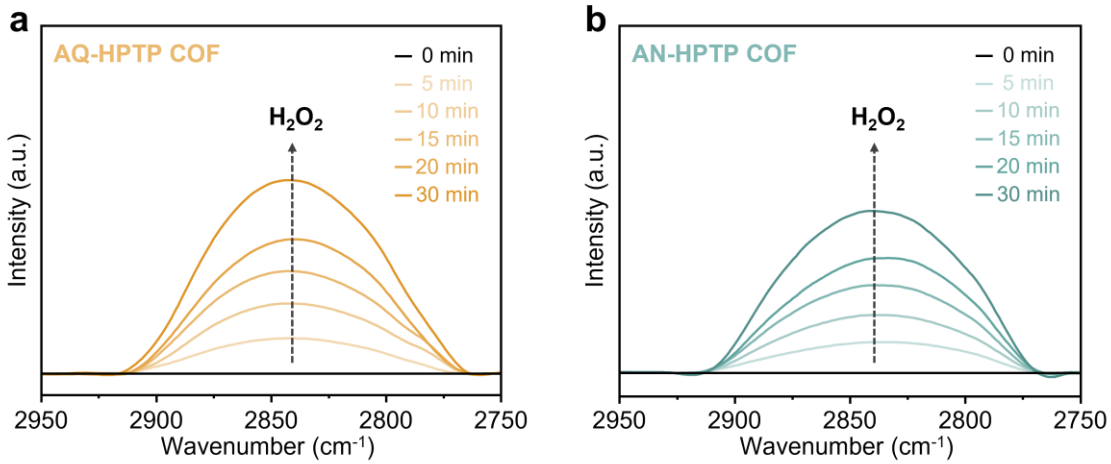

Figure S11. In situ DRIFTS spectra obtained on (a) AQ-HPTP COF and (b) AN-HPTP COF under visible light irradiation (λ>420 nm, 300 W Xe lamp).

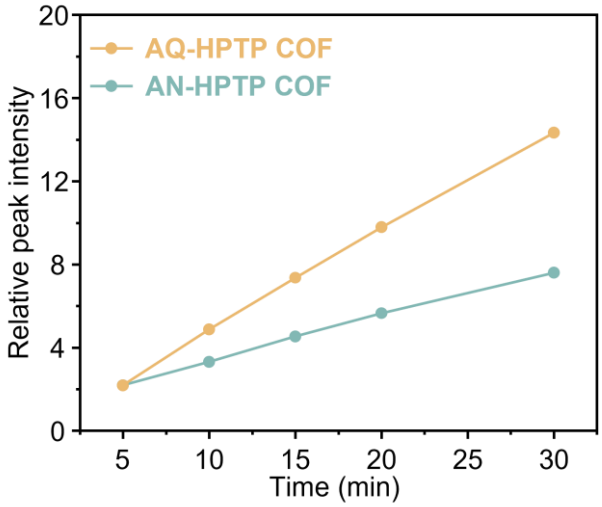

Figure S12. Time-dependent variations of normalized relative peak intensities as shown in Figure S11.

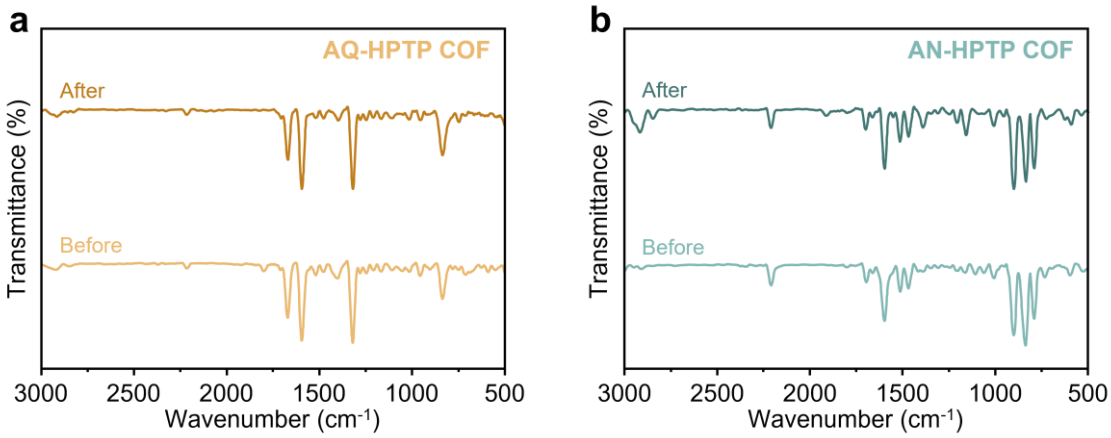

Figure S13. FTIR spectra of (a) AQ-HPTP COF and (b) AN-HPTP COF obtained after multiple photocatalytic cycles along with that before photocatalysis.

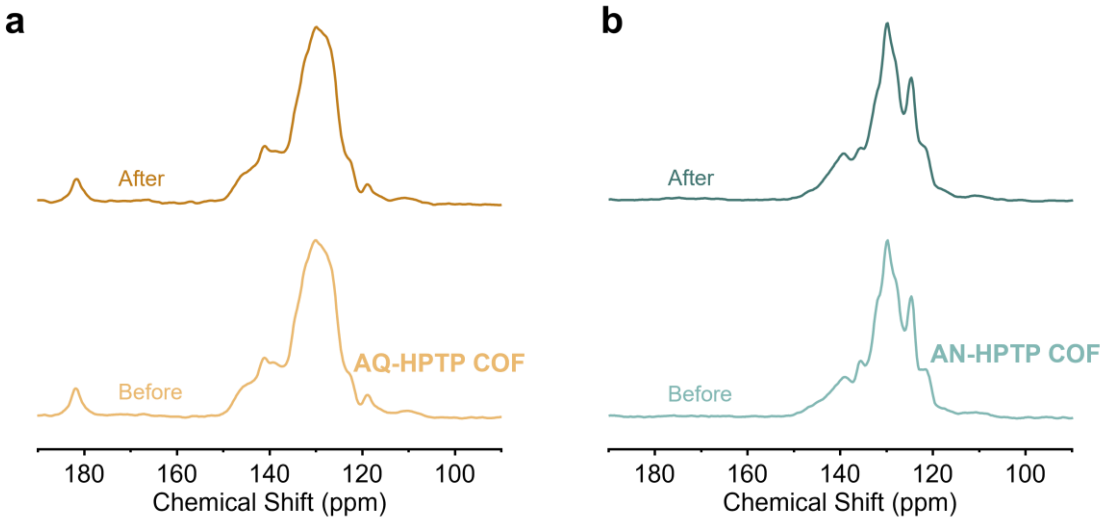

Figure S14. Solid state ^{13}C CP-MAS NMR spectra of (a) AQ-HPTP COF and (b) AN-HPTP COF obtained after multiple photocatalytic cycles along with that before photocatalysis.

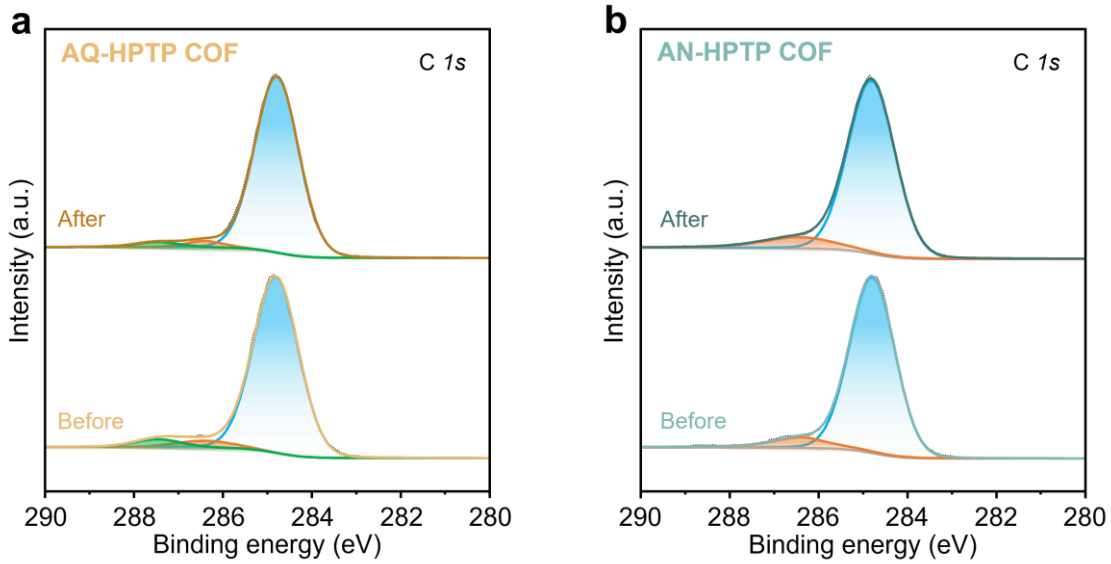

Figure S15. High-resolution C *1s* XPS spectra of(a) AQ-HPTP COF and (b) AN-HPTP COF obtained after multiple photocatalytic cycles along with that before photocatalysis.

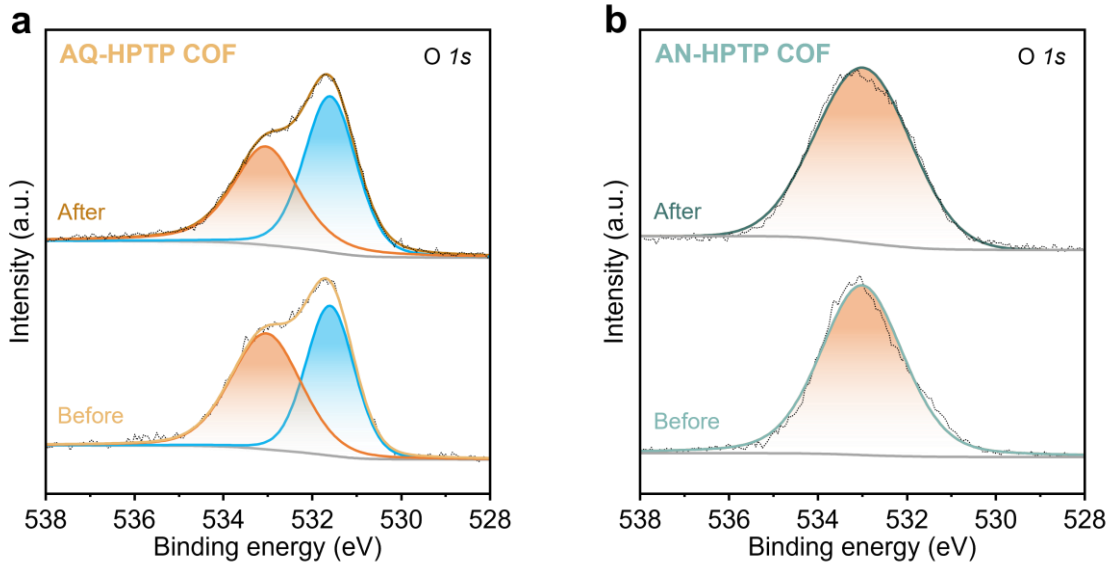

Figure S16. High-resolution O *1s* XPS spectra of (a) AQ-HPTP COF and (b) AN-HPTP COF obtained after multiple photocatalytic cycles along with that before photocatalysis.

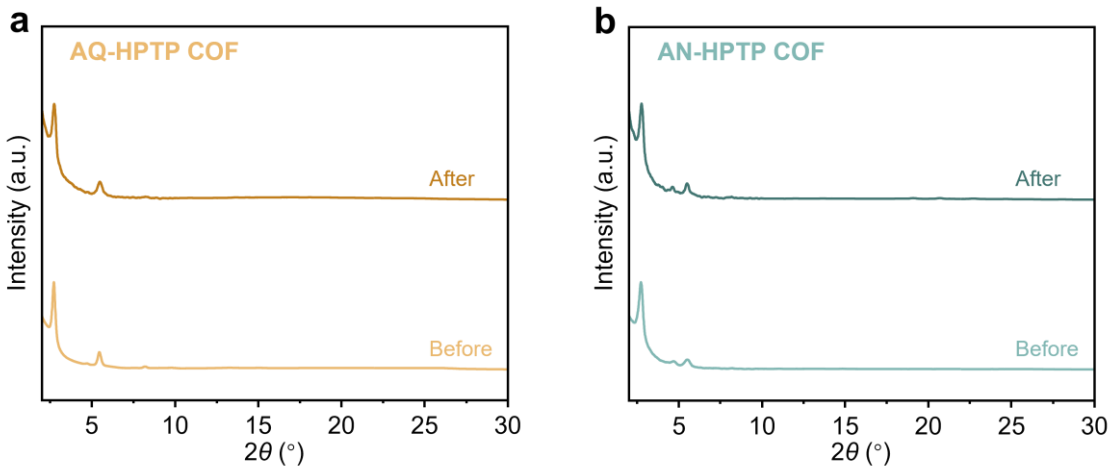

Figure S17. PXRD patterns of (a) AQ-HPTP COF and (b) AN-HPTP COF obtained after multiple photocatalytic cycles along with that before photocatalysis.

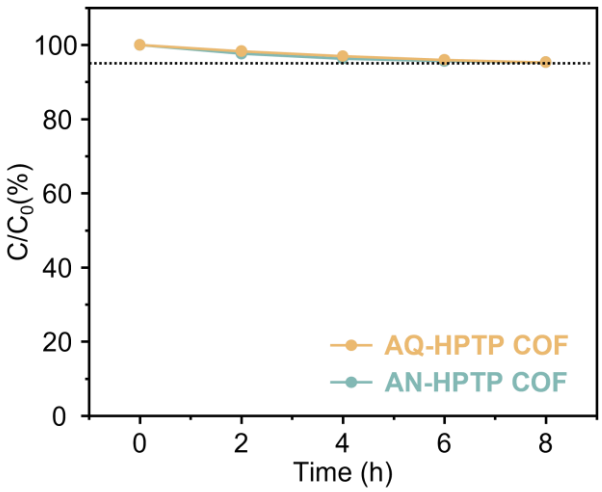

Figure S18. Photocatalytic decomposition of H_2O_2 (C_0=1 mM) in pure water under visible light irradiation (λ>420 nm, 300 W Xe lamp) over AQ-HPTP COF and AN-HPTP COF.

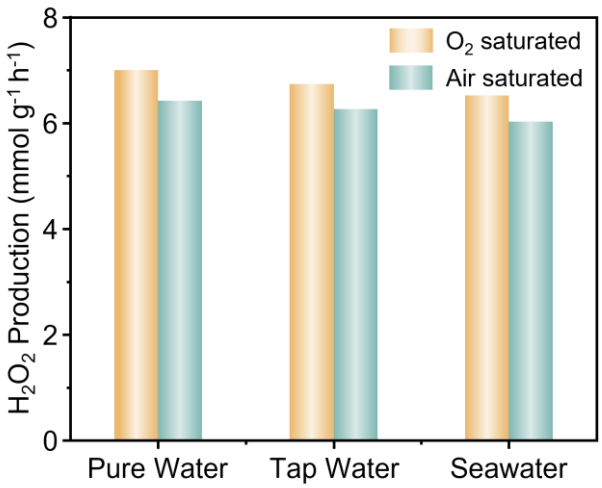

Figure S19. The photosynthetic H_2O_2 production performance in O_2- and air-saturated pure water, tap water, and seawater under visible light irradiation ($\lambda > 420$ nm, 300 W Xe lamp) using AQ-HPTP COF.

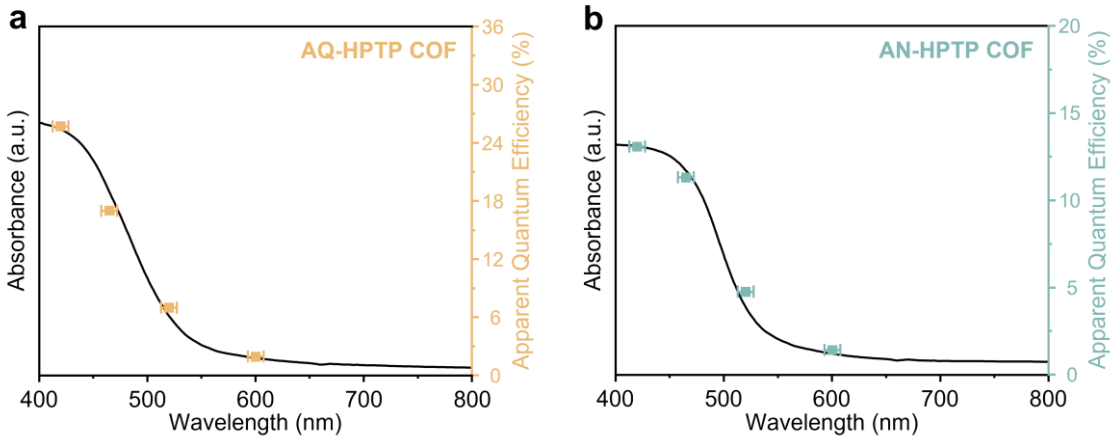

Figure S20. Wavelength-dependent AQEs of (a) AQ-HPTP COF and (b) AN-HPTP COF. The UV-vis absorption spectra of the photocatalysts are superimposed for comparison.

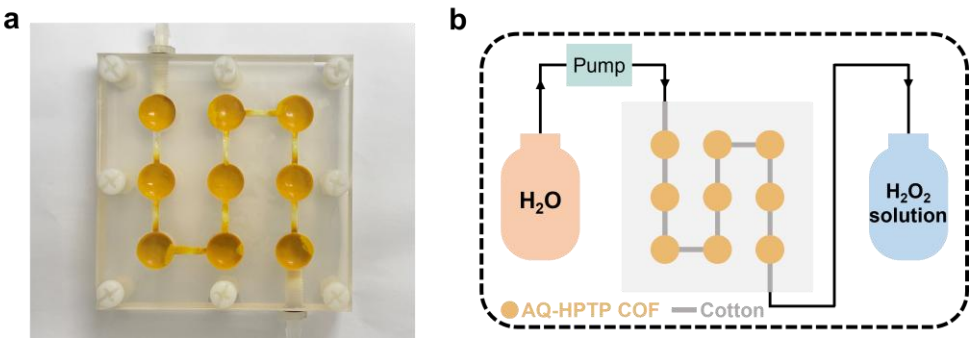

Figure S21. (a) Photograph of the flow reactor and (b) schematic of the continuous-flow photocatalytic reactor.

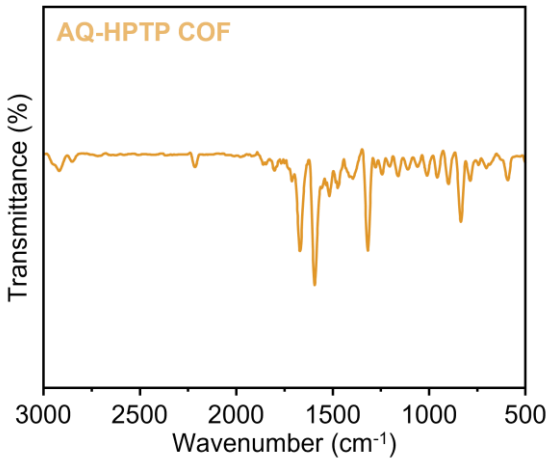

Figure S22. FTIR spectrum of AQ-HPTP COF after continuous-flow photocatalytic reaction.

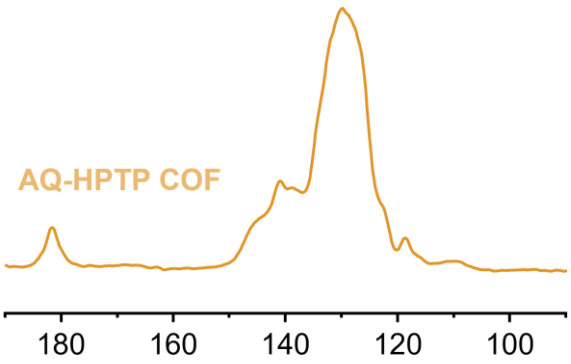

Figure S23. Solid state ^{13}C CP-MAS NMR spectra of AQ-HPTP COF after continuous-flow photocatalytic reaction.

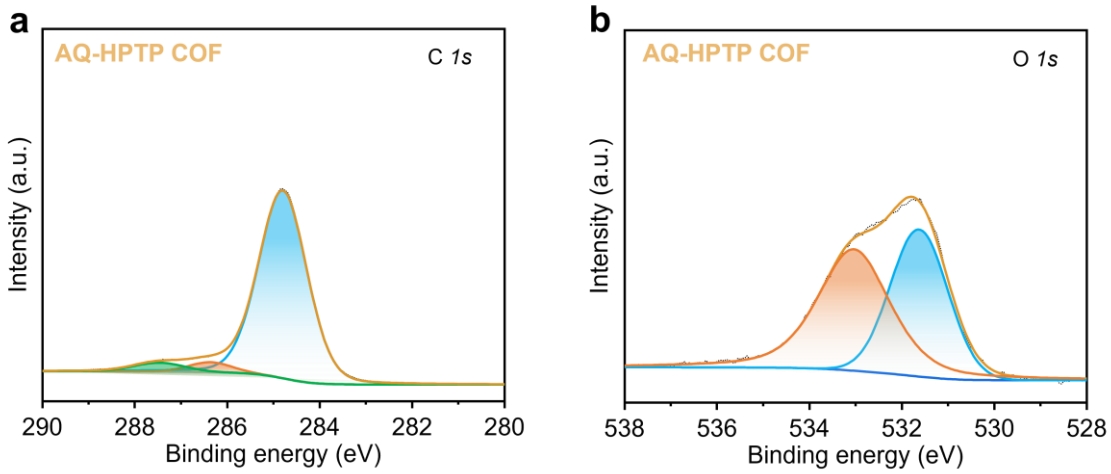

Figure S24. High-resolution (a) C *1s* and (b) O *1s* XPS spectra of AQ-HPTP COF after continuous-flow photocatalytic reaction.

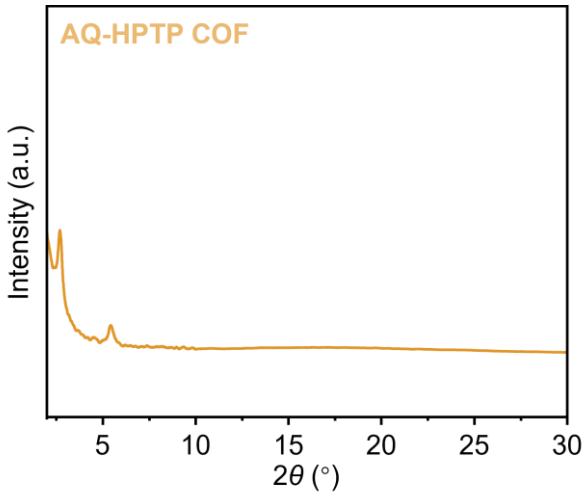

Figure S25. PXRD patterns of AQ-HPTP COF after continuous-flow photocatalytic reaction.

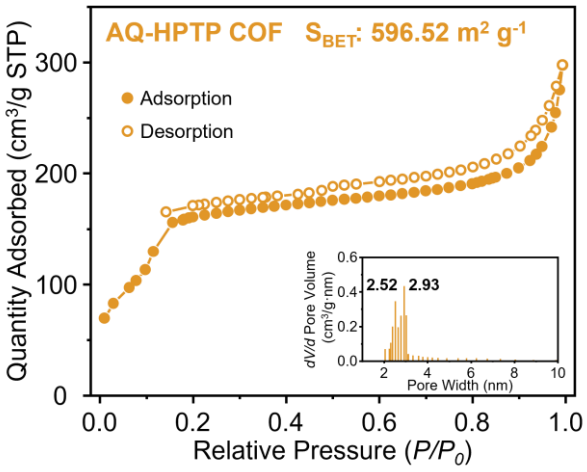

Figure S26. N_2 adsorption/desorption isotherms of AQ-HPTP COF after continuous-flow photocatalytic reaction.

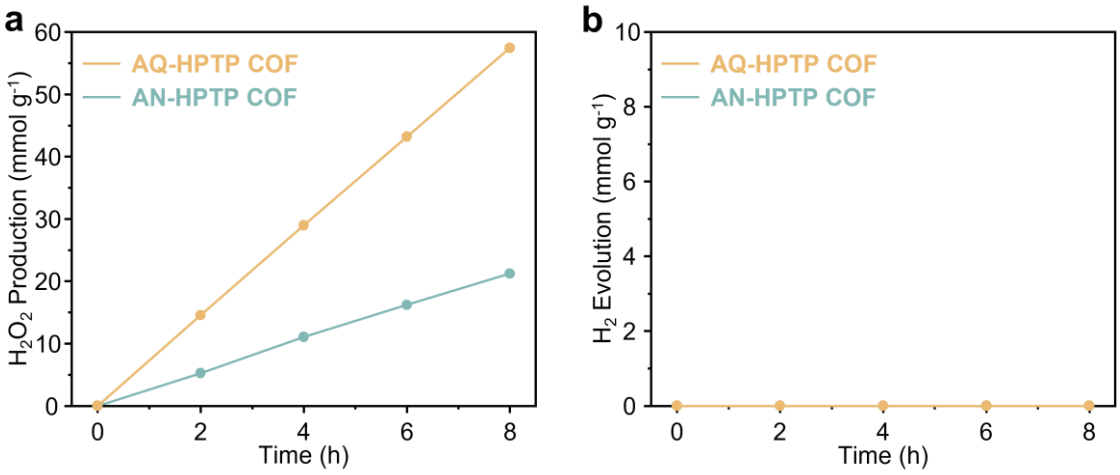

Figure S27. Time-dependent (a) H_2O_2 formation under O_2 atmosphere and (b) H_2 formation under Ar atmosphere for AQ-HPTP COF and AN-HPTP COF using methanol as the sacrificial agent.

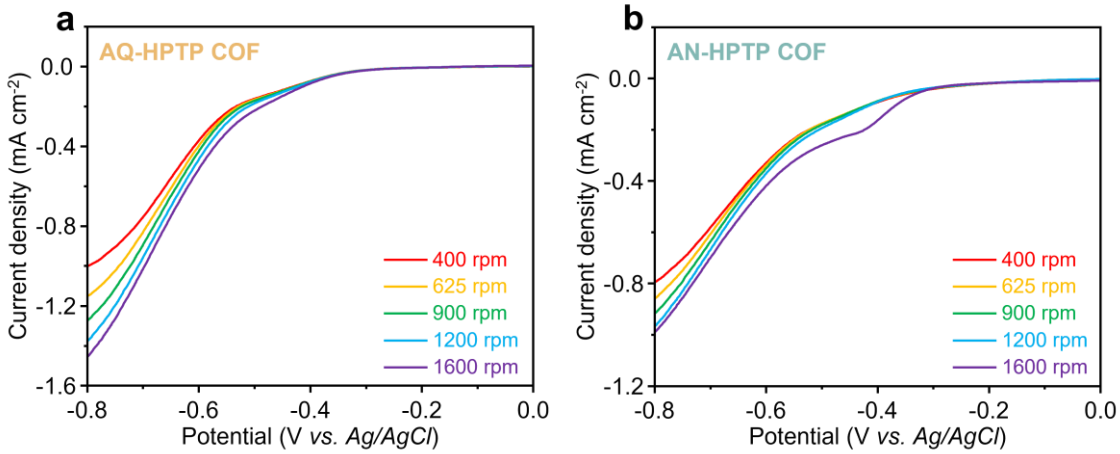

Figure S28. Different rotating speeds of linear-sweep RDE voltammograms of (a) AQ-HPTP COF and (b) AN-HPTP COF under visible light irradiation (λ>420 nm, 300 W Xe lamp).

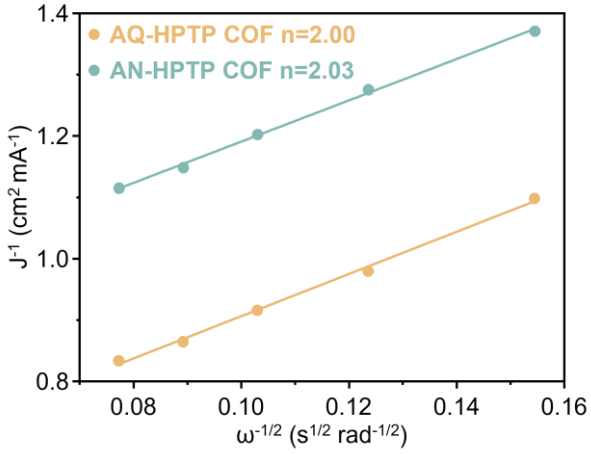

Figure S29. The Koutecky–Levich plots of AQ-HPTP COF and AN-HPTP COF obtained by RDE measurements at approximately −0.80 V (vs Ag/AgCl) under visible light irradiation (λ >420 nm, 300 W Xe lamp).

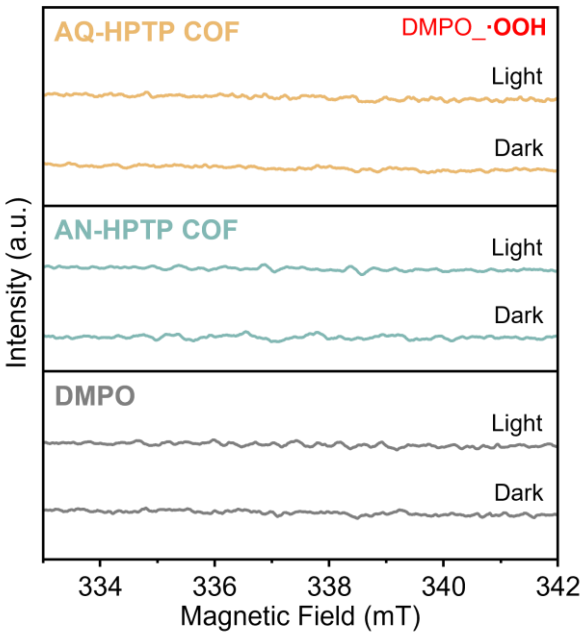

Figure S30. EPR spectra of AQ-HPTP COF and AN-HPTP COF in the presence of DMPO under O_2 atmosphere with and without visible light irradiation (λ >420 nm, 300 W Xe lamp).

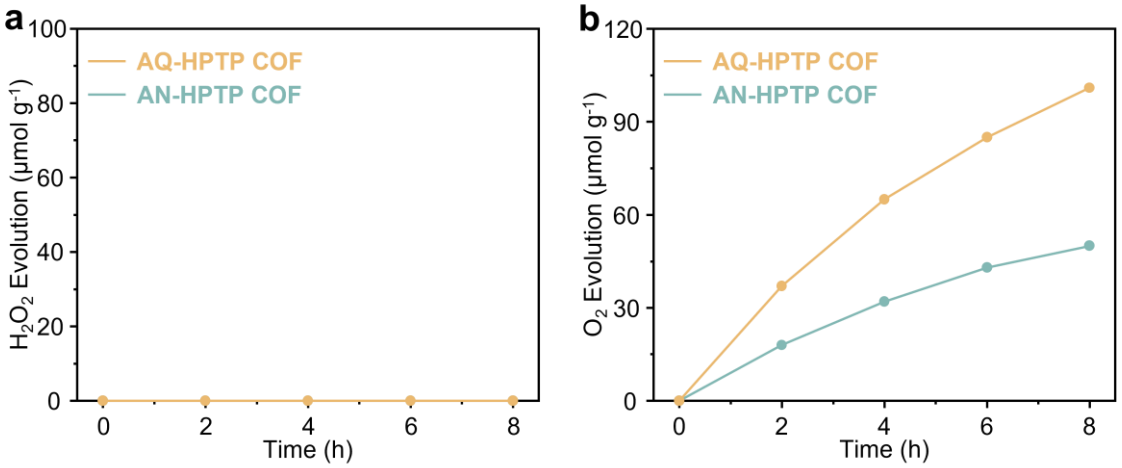

Figure S31. Time-dependent (a) H_2O_2 formation and (b) O_2 formation under Ar atmosphere for AQ-HPTP COF and AN-HPTP COF using $NaIO_3$ as the electron acceptor.

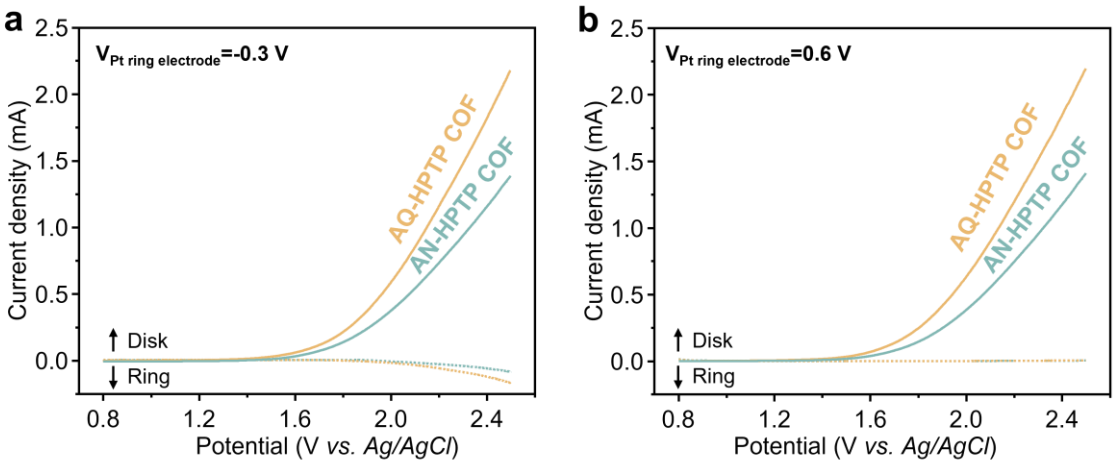

Figure S32. RRDE voltammograms of AQ-HPTP COF and AN-HPTP COF obtained in 0.1 M phosphate buffer solution (pH=7) with a scan rate of 10 mV s^{-1} and a rotation rate of 1000 rpm under visible-light irradiation (λ>420 nm, 300 W Xe lamp). The potential of the Pt ring electrode was set at (a) -0.3 V versus Ag/AgCl to detect O_2 and (b) 0.6 V versus Ag/AgCl to detect H_2O_2. During RRDE measurements, the reduction current observed at the Pt ring electrode at a constant potential of -0.3 V (versus Ag/AgCl) indicates the capacity of both COFs to produce O_2 through the WOR. On the other hand, the absence of an oxidation current at 0.6 V (versus Ag/AgCl) at the Pt ring electrode excludes the formation of H_2O_2 via the WOR.

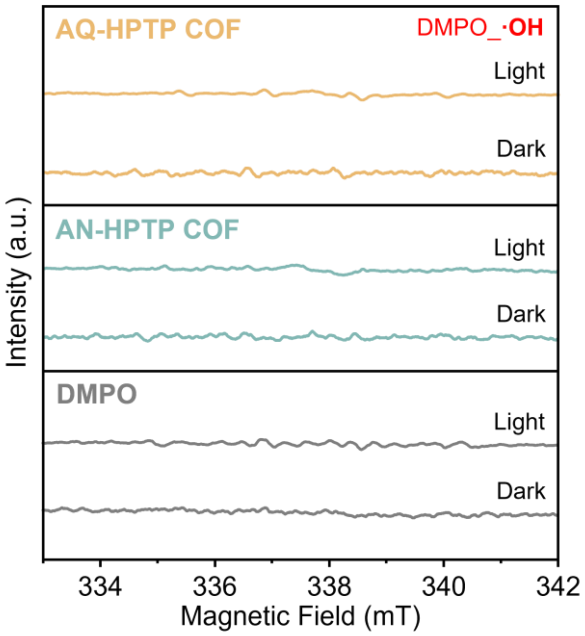

Figure S33. EPR spectra of AQ-HPTP COF, AN-HPTP COF, and DMPO in $NaIO_3$ aqueous solutions (0.01 M) under Ar atmosphere with and without visible light irradiation (λ>420 nm, 300 W Xe lamp). DMPO-•OH spin adducts are not detected in both COFs under the Ar atmosphere, suggesting that the stepwise one-electron water oxidization pathway for H_2O_2 production is also excluded.

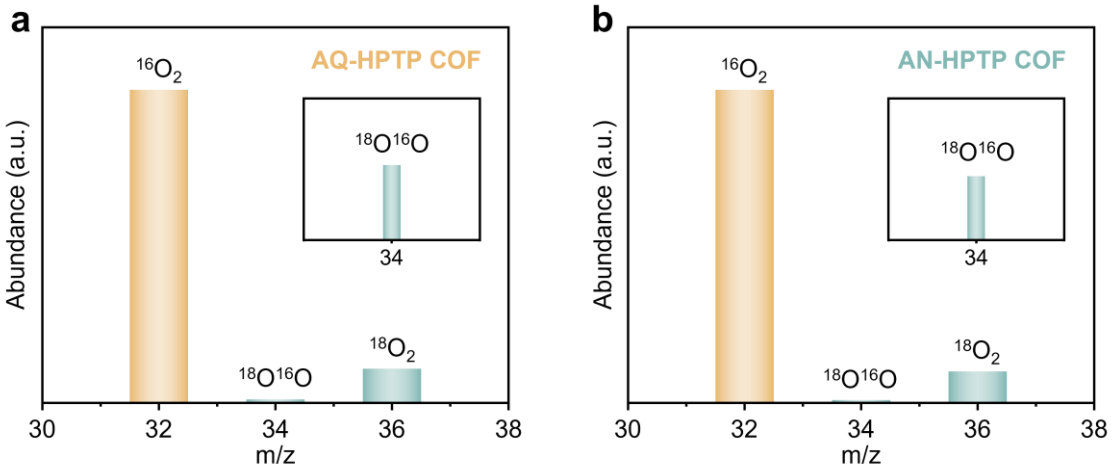

Figure S34. GC-MS spectra of the gas extracted from the (a) AQ-HPTP COF and (b) AN-HPTP COF in $H_2{}^{18}O$ system after the visible-light irradiation (λ>420 nm, 300 W Xe lamp) for 1 h and catalase enzyme treatment.

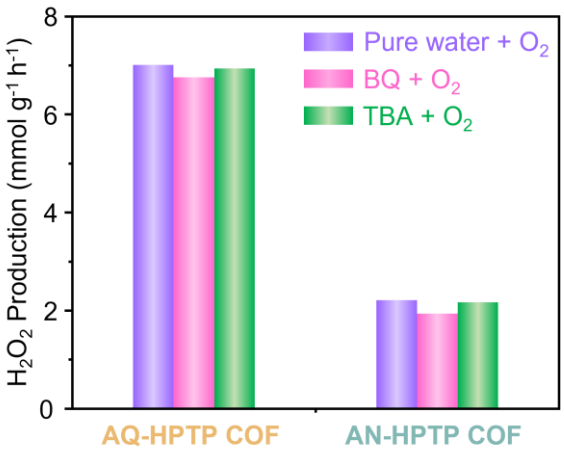

Figure S35. Comparison of the photocatalytic H_2O_2 production performance for AQ-HPTP COF and AN-HPTP COF in the presence of different scavengers (BQ as the superoxide radical quencher and TBA as the hydroxyl radical scavenger).

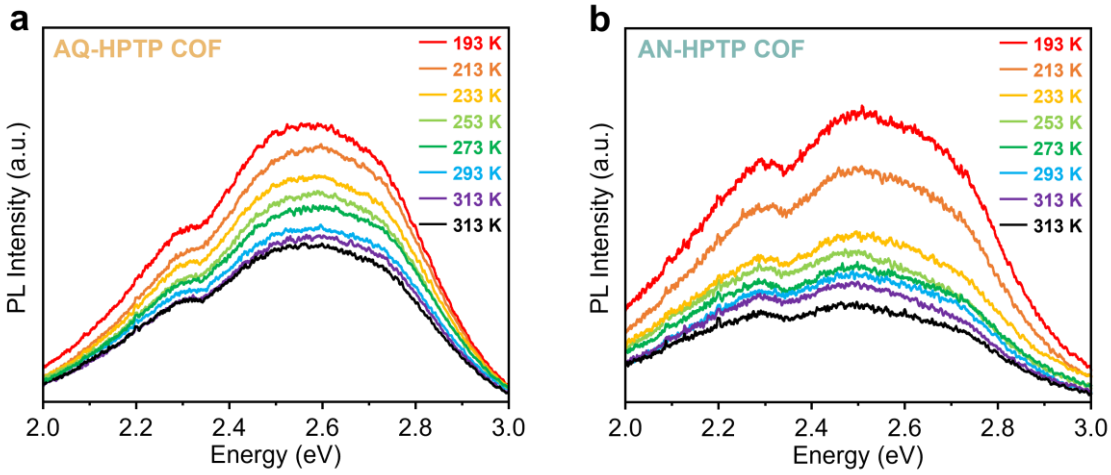

Figure S36. Temperature-dependent PL spectra of (a) AQ-HPTP COF and (b) AN-HPTP COF.

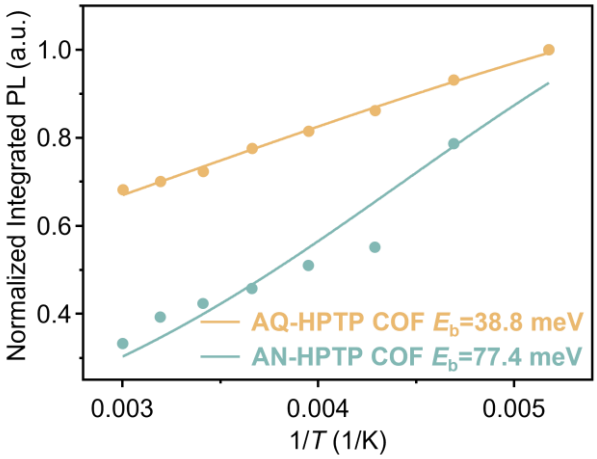

Figure S37. Normalized integrated PL intensities of AQ-HPTP COF and AN-HPTP COF obtained from temperature-dependent PL measurements. The solid lines represent the exponential fitting of the data points.

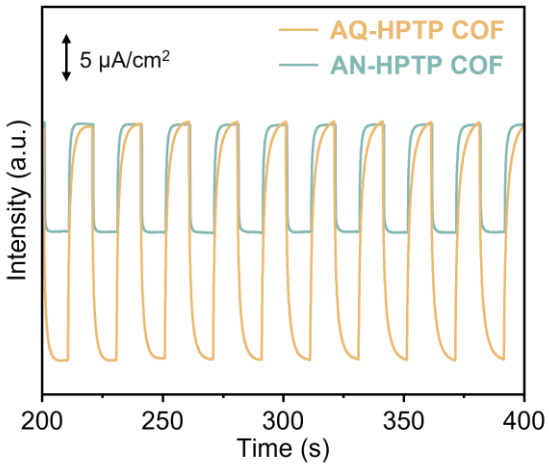

Figure S38. Transient photocurrent measurements of AQ-HPTP COF and AN-HPTP COF under visible light irradiation (λ>420 nm, 300 W Xe lamp).

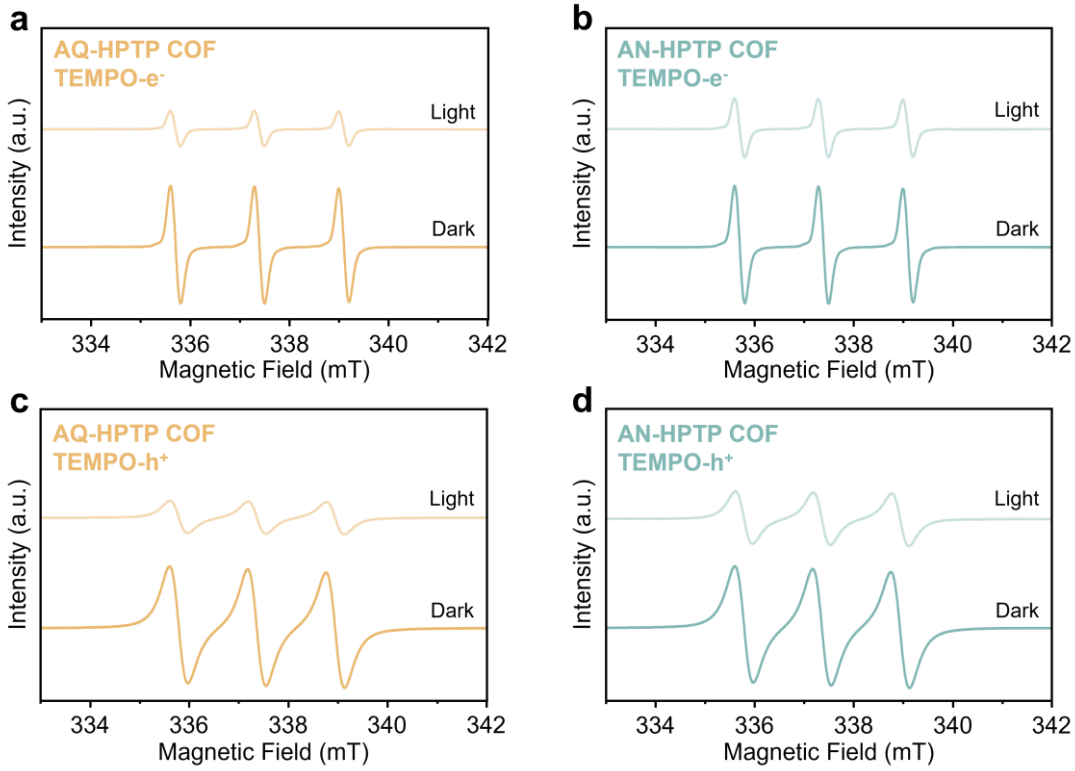

Figure S39. EPR spectra of detecting photogenerated electrons in an aqueous solution of (a) AQ-HPTP COF and (b) AN-HPTP COF with and without visible light irradiation (λ>420 nm, 300 W Xe lamp). EPR spectra of detecting photogenerated holes in an acetonitrile solution of (a) AQ-HPTP COF and (b) AN-HPTP COF with and without visible light irradiation (λ>420 nm, 300 W Xe lamp).

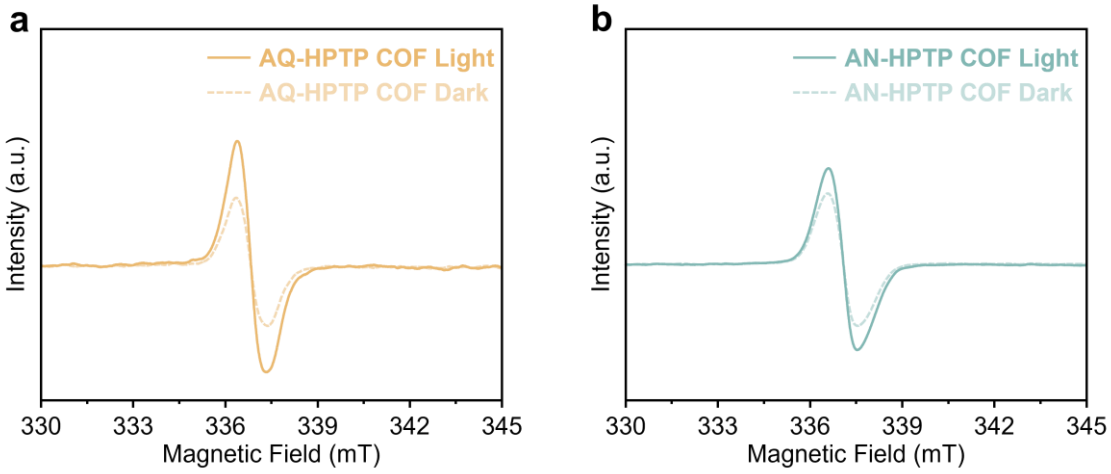

Figure S40. Solid state EPR spectra of (a) AQ-HPTP COF and (b) AN-HPTP COF with and without visible light irradiation (λ>420 nm, 300 W Xe lamp).

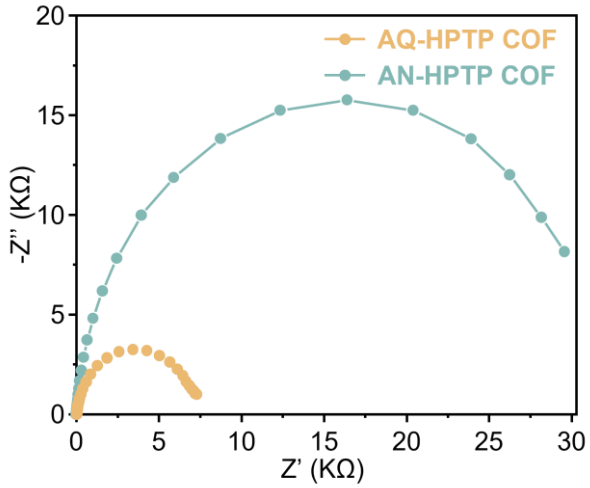

Figure S41. EIS Nyquist plots of AQ-HPTP COF and AN-HPTP COF under visible light irradiation (λ>420 nm, 300 W Xe lamp).

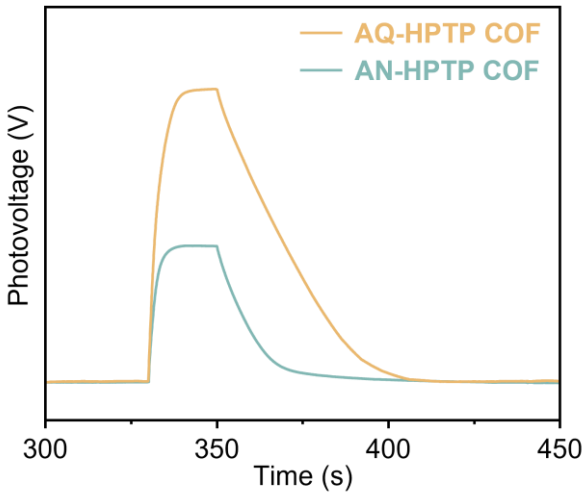

Figure S42. Transient open-circuit voltage decay (OCVD) measurements of AQ-HPTP COF and AN-HPTP COF under visible light irradiation (λ>420 nm, 300 W Xe lamp).

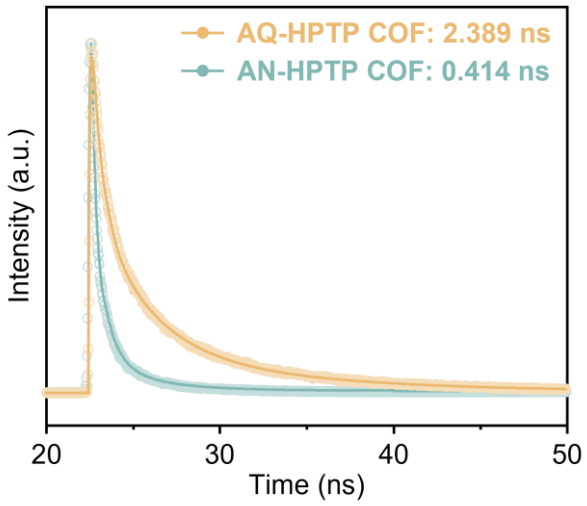

Figure S43. Time-correlated single photon counting (TCSPC) measurements of AQ-HPTP COF and AN-HPTP COF together with fitting results.

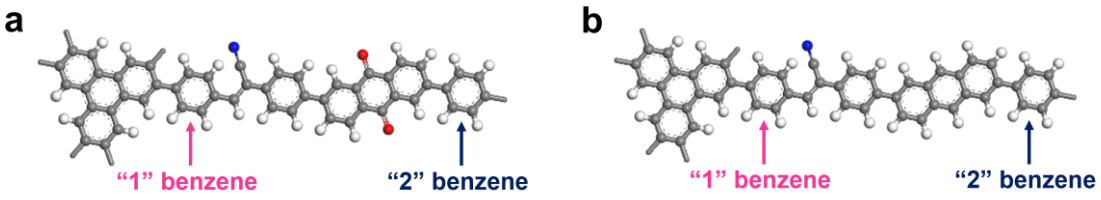

Figure S44. The structure fragment of (a) AQ-HPTP COF and (b) AN-HPTP COF.

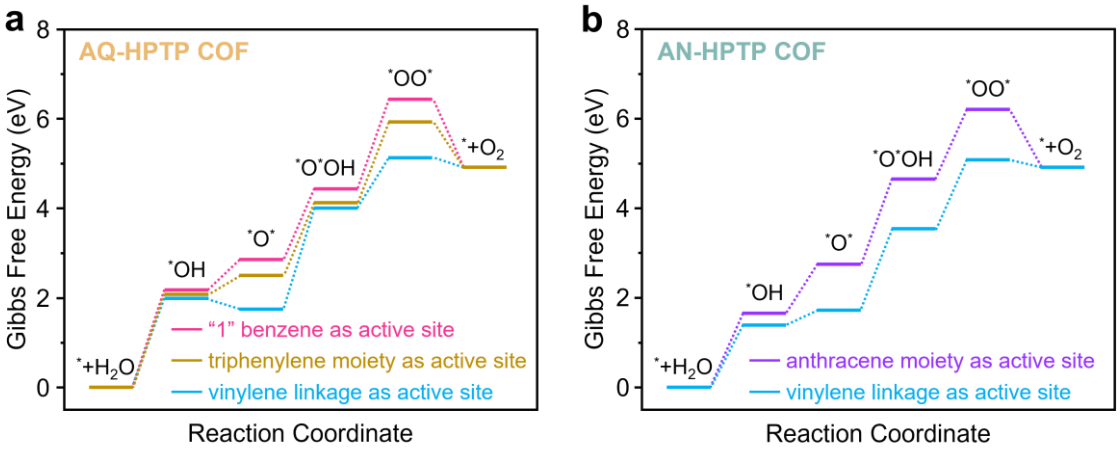

Figure S45. Calculated free energy diagrams of water oxidation pathway on differnet active sites in (a) AQ-HPTP COF and (b) AN-HPTP COF.

References

[1] W. Zhang, M. Sun, J. Cheng, X. Wu, H. Xu, *Adv. Mater.* **2025**, *37*, 2500913.

[2] G. Kresse, J. Hafner, *Phys. Rev. B Condens. Matter* **1993**, *47*, 558.

[3] G. Kresse, J. Furthmüller, *Comp. Mate. Sci*. **1996**, *6*, 15.

[4] J. P. Perdew, K. Burke, M. Ernzerhof, *Phys. Rev. Lett.* **1996**, *77*, 3865.

[5] P. E. Blochl, P*hys. Rev. B Condens. Matter* **1994**, *50*, 17953.

[6] G. Kresse, D. Joubert, *Phys. Rev. B* **1999**, *59*, 1758.

[7] J. Heyd, G. E. Scuseria, *J. Chem. Phys.* **2004**, *121*, 1187.

[8] V. Wang, N. Xu, J. Liu, G. Tang, W. Geng, *Comput. Phys. Commun.* **2021**, *267*, 108033.

[9] E. Skúlason, G. S. Karlberg, J. Rossmeisl, T. Bligaard, J. Greeley, H. Jónsson, J. K. Nørskov, *Phys. Chem. Chem. Phys.* **2007**, *9*, 3241.